Circulation in the Alboran Sea as Determined by Quasi-Synoptic Hydrographic Observations. Part I: Three-Dimensional Structure of the Two Anticyclonic Gyres

ÁLVARO VIÚDEZ* AND JOAQUÍN TINTORÉ

Departament de Física, Universitat de les Illes Balears, Palma de Mallorca, Spain

ROBERT L. HANEY

Department of Meteorology, Naval Postgraduate School, Monterey, California

(Manuscript received 14 October 1993, in final form 18 April 1995)

ABSTRACT

The circulation and dynamics of the Modified Atlantic Water have been studied using data from an intensive field experiment carried out between 22 September and 7 October 1992. Data included 134 CTD casts, ADCP, and satellite imagery. A well-defined wavelike front was observed with two significant anticyclonic gyres in the western and eastern Alboran Sea. Smaller-scale cyclonic eddies were also observed. The front separates the more saline, older modified Atlantic water ($S > 38$) in the northern region from the fresher, more recent modified Atlantic water ($S < 36.8$) in the south. The associated baroclinic jet had a mean transport of 1 Sv and maximum geostrophic velocities of 1.0 m s^{-1}. The three-dimensional structure and spatial scales of both gyres were similar, that is, 90 km long and 220 m deep. In the eastern Alboran, northeast of Oran, the origin of the Algerian Current was also detected with an eastward transport of 1.8 Sv. The general picture can be presented as a structure formed by a wavelike front coupled with two large anticyclonic gyre–small cyclonic eddy systems.

The relative importance of stratification, relative vorticity, and Froude number in the distribution of Ertel's potential vorticity has been examined, and potential vorticity conservation is used to infer vertical motion. The vertical velocity forcing has been computed using the quasigeostrophic Q vector formulation of the omega equation. It is found that the differential vorticity advection due to mesoscale phenomena in the western Alboran plays a main role in this forcing. The vertical velocities associated with these mesoscale structures reach maximum absolute values of 15 m day^{-1}.

1. Introduction

The Mediterranean Sea is a semienclosed basin whose large-scale circulation is mainly controlled by the excess of evaporation over the freshwater input from precipitation and rivers. A two-layer flow through the Strait of Gibraltar compensates for the water and salt deficit with Atlantic water (AW, $S < 36.5$) flowing in the upper layer into the Alboran Sea and Mediterranean Water (MW, $S > 38.4$) flowing westward below. Being the westernmost Mediterranean subbasin, the Alboran Sea is the first to receive the incoming AW. The AW is modified in the Alboran Sea, acquiring characteristics intermediate between the underlying MW and the AW, and is termed modified Atlantic water (MAW) or Atlantic–Mediterranean Interface Water (A–MIW, Gascard and Richez 1985).

The dynamics associated with the incoming AW in the Alboran Sea has been described in several field experiments. The large anticyclonic gyre that is formed west of Cape Tres Forcas [the western Alboran gyre (WAG)] was discovered in the late 1960s (Seco 1959; Donguy 1962). Lanoix (1974) from one month of ship data obtained the dynamic topography field for the entire Alboran subbasin, showing the WAG and an eastward current along the Moroccan coast in the eastern Alboran. After several field experiments in the western Alboran (Cano and de Castillejo 1972; Gascard and Richez 1985; Heburn and La Violette 1990; Tintoré et al. 1991) including recent international experiments such as Donde Va? in 1982 (Donde Va? Group 1984; La Violette 1986; Parrilla and Kinder 1987) and the Western Mediterranean Circulation Experiment in 1986 (La Violette 1990) the WAG is considered a quasi-permanent feature. More recently, studies concerned with the inflow variability (Perkins et al. 1990) and mesoscale cyclonic eddies (Tintoré et al. 1991) have clarified the dynamical description of the

* Current affiliation: Department of Meteorology, Naval Postgraduate School, Monterey, California.

Corresponding author address: Álvaro Viúdez, Naval Postgraduate School, Dept. of Meteorology, Room 253, 589 Dyer Road, Monterey, CA 93943-5114.

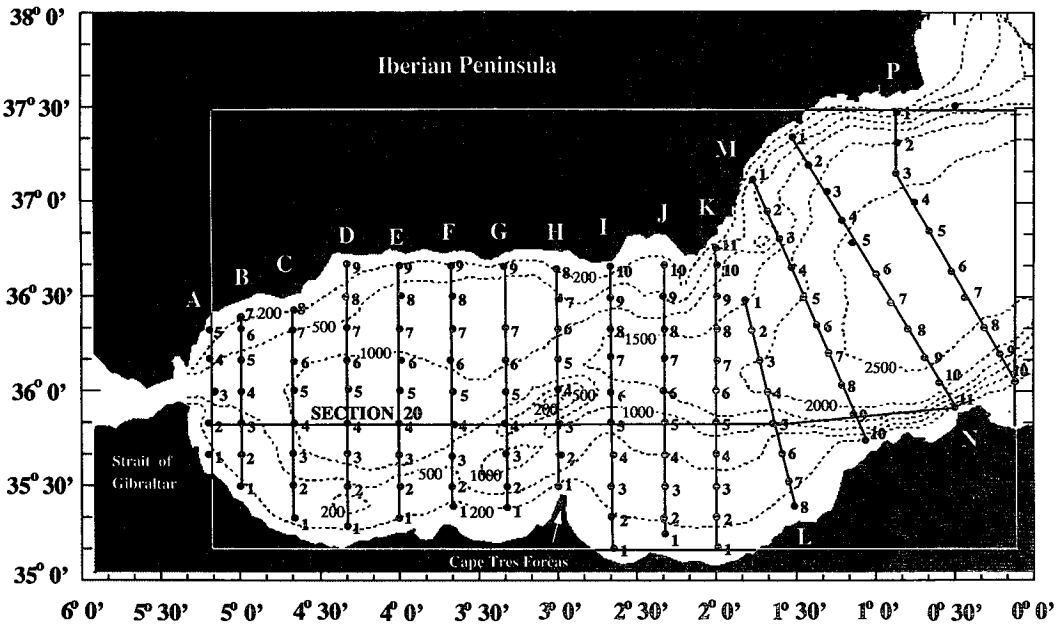

FIG. 1. The Alboran Sea (bottom topography in m). The different vertical CTD sections are referenced.

western Alboran addressing the importance of mesoscale features. An exhaustive recent summary of the field and numerical experiments can be found in Speich (1992).

In the eastern Alboran Sea less information is available, but several studies (Lanoix 1974; Cheney 1978; Cheney and Doblar 1982; Heburn and La Violette 1990; Viúdez and Tintoré 1995) have shown that a second anticyclonic gyre [the eastern Alboran gyre (EAG)] or an eastward current along the Moroccan coast can be present. Variations in the structure of the WAG and EAG have been studied by Heburn and La Violette (1990) from satellite imagery, showing that the disappearance of either gyre occurs on a timescale of one to two weeks. In the easternmost Alboran, an intense density front (Almería–Oran Front) is sometimes present, which appears to be partly influenced by the size and position of the EAG (Tintoré et al. 1988; Arnone et al. 1990).

In summary, the large-scale circulation of the MAW in the Alboran Sea shows the presence of an eastward jet, and one or two large anticyclonic gyres lying in the western and eastern Alboran Basin. At smaller scales, jet fluctuations and eddies distort this large-scale picture. Both gyres, the jet, and the Almería–Oran front were always studied as individual systems (with the exception of the satellite imagery studies), and as a result, a quasi-synoptic 3D dynamical study of the entire Alboran Basin was never carried out. The goal of this work is to present the quasi-synoptic physical characteristics, with emphasis on the importance of the mesoscale dynamics (and especially the vertical motions) in the entire Alboran Sea system. With such a purpose we carried out a field experiment over a high-resolution regular grid (20′ longitude × 10′ latitude) covering the Alboran Sea. We describe how the data were obtained in section 2. From these data we compute the dynamic fields (section 3), the potential vorticity distribution (section 4), and the quasigeostrophic vertical velocities using the omega equation (section 5).

2. Data

The field experiment was carried out from 17 September to 7 October 1992, on board the R/V *García del Cid.* From 18 to 19 September we sampled the first eight stations (Fig. 1) using a Neil Brown Mark III CTD. For ease of reference we denote the south–north vertical sections using a letter (from A to P), and each station is then identified by the letter of its vertical section plus a number (Fig. 1). Due to a failure in the CTD reception system the casts continued with a Sea Bird SBE-25 CTD from 21 September (first station, A01) to 7 October resulting in 134 stations in a quasi-regular grid covering the entire Alboran Sea. Distance between stations was usually 20′ longitude × 10′ latitude (~30 × 18 km). The vertical profiles were made to 600 m except in coastal regions and in vertical sections D and K where they reached the bottom. The vertical resolution of each CTD profile after filtering and interpolation was 1 m. In addition, continuous sur-

face temperature and salinity data were collected. Horizontal components of velocity were continuously monitored using a ship-mounted ADCP with vertical resolution of 8 m and a maximum depth of 300 m. Five-minute averages were carried out while under way, implying a resolution of 1.5 km. Satellite imagery for the period 12 September–11 October has been also analyzed. Eight NOAA 11 and NOAA 9 AVHRR (Advanced Very High Resolution Radiometer) images were selected (channel 4) and represent relative sea surface temperature. All selected images were geographically located.

3. Observations

At large scale, the density field exhibits a wavelike pattern with two bowls of warm and less saline water. The temperature, salinity, and density distributions at 100 m are shown in Fig. 2. Maximum horizontal gradients of the front at this depth are 1.5°C, 1.2 psu, and 2 σ_t in about 20 km, gradients being stronger in the western Alboran (~4°00′W). The wavelike front, a result of the incoming Atlantic inflow at the Strait of Gibraltar, separates older MAW (colder and more saline, and therefore denser) located in the northern Alboran Sea from the more recent MAW (warmer and less saline, and therefore less dense) located in the south. The front extends from Gibraltar to the eastern Alboran Basin reaching the African coast the first time west of Cape Tres Forcas (3°20′W) and the second time near Oran (0°30′W) where the Algerian Current begins.

The two large bowls of warmer and lighter water embedded in the southern part of the front are the WAG and EAG. Two mesoscale eddies located southwest of each anticyclonic gyre are also clearly observed between the gyres and the coast. North of the front is a region of homogeneous temperature and salinity (with some exception in the northeastern most sampled region at 37°N, 1°W). In summary, the density field presents a wavelike front coupled with two anticyclonic gyre–cyclonic eddy systems.

A clear characteristic of both gyres is the large vertical thickness of the homogeneous salinity layer of recent advected MAW (with $S < 36.6$), which occupies a considerable part of the gyres (Fig. 3). The vertical temperature gradients, however, remain significant here. These characteristics have their origin in the vertical structure of the surface Atlantic inflow (Fig. 4), which presents a homogeneous salinity layer but with vertical temperature gradients. This Atlantic inflow near the Strait of Gibraltar exhibits a well-known (Gascard and Richez 1985) subsurface relative salinity minimum ($S < 36.5$). This relative salinity minimum flows out of the Strait of Gibraltar throughout the Alboran Sea and can be used as a tracer, since, assuming homogeneous mixing, the relative minimum does not lose its relative minimum condition although its absolute salinity value will increase by local mixing (salinity gradients will decrease also). A scheme of this feature is represented in Fig. 5. Although a full exploitation of this feature to map the mean particle trajectories requires a denser sampling, several questions arise from our observations. Subsurface salinity minima following a 3D path are not easy to visualize, but from Fig. 6 we

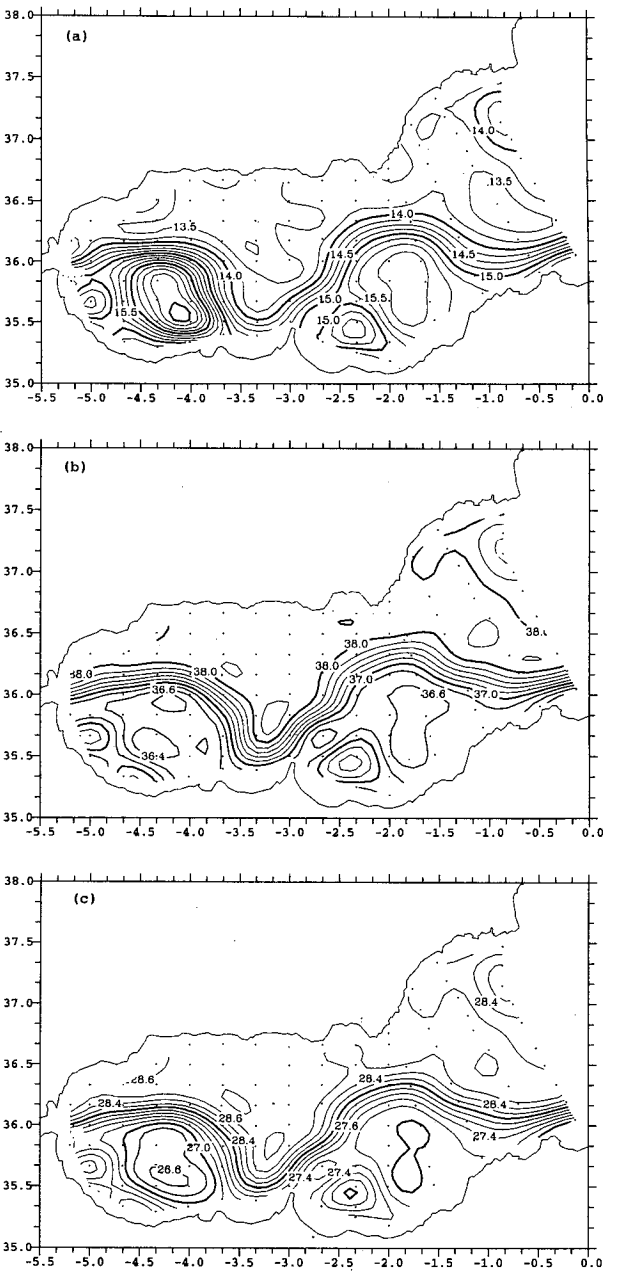

FIG. 2. (a) Temperature ($\Delta = 0.25$°C), (b) salinity ($\Delta = 0.2$ psu), and (c) σ_t ($\Delta = 0.2\ \sigma_t$) horizontal distributions at 100 m. Interpolation method: successive corrections (referenced in the text).

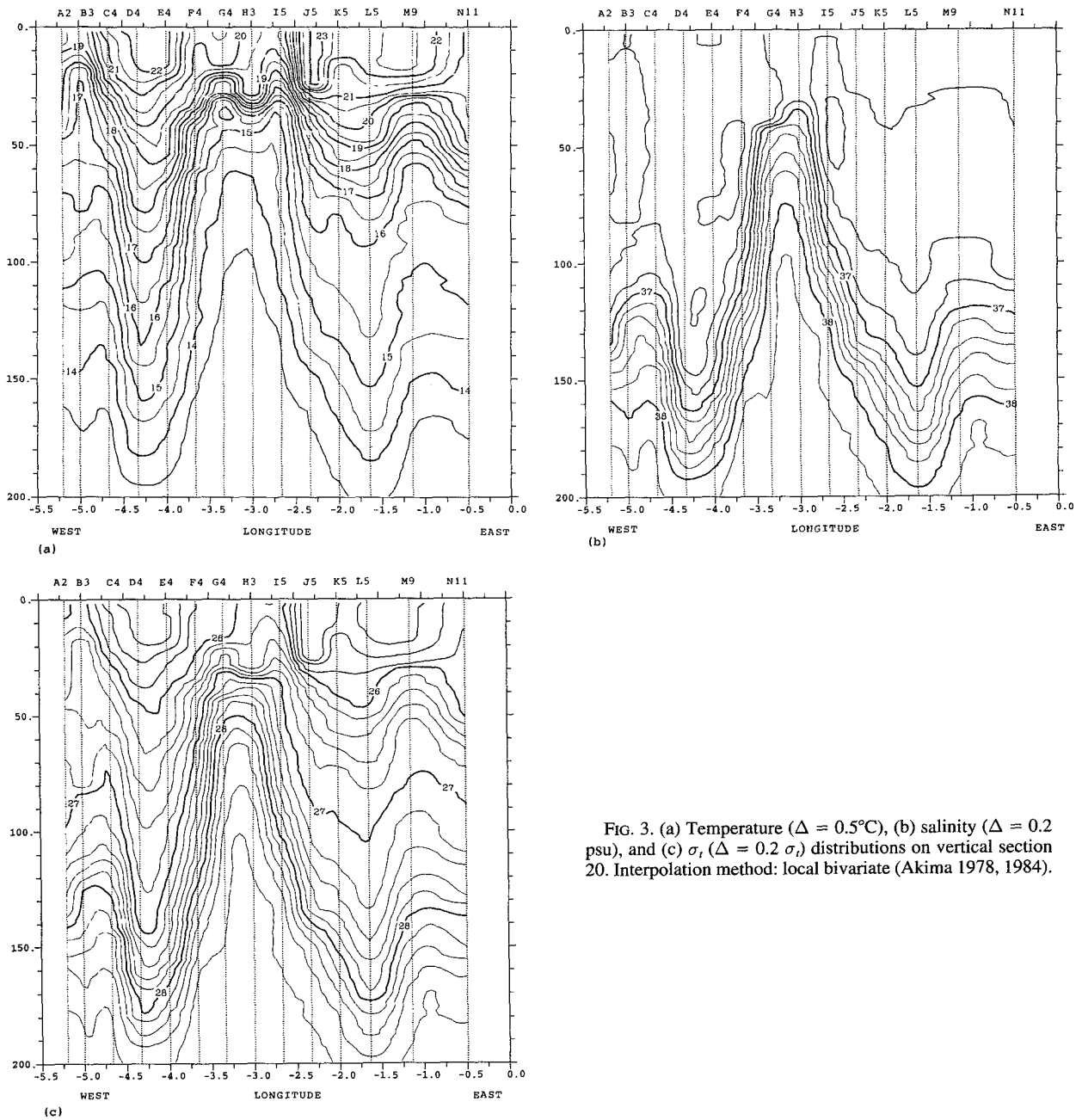

FIG. 3. (a) Temperature (Δ = 0.5°C), (b) salinity (Δ = 0.2 psu), and (c) σ_t (Δ = 0.2 σ_t) distributions on vertical section 20. Interpolation method: local bivariate (Akima 1978, 1984).

can infer the different depths and locations of the water with salinity values less than 36.45 psu. Initially, the minimum appears in the Atlantic jet near the Strait of Gibraltar between 0 and 100 m depth. Eastward the minimum fills the core of the WAG from 50 to 150 m. Next, this water is observed between 10 and 40 m near the African coast, west of Cape Tres Forcas, where the flow acquires a northeastward direction, and then follows an anticyclonic path in the EAG at ~50 m depth, which is observed in an intermittent way due to the discrete sampling. The core of the EAG also has a subsurface salinity minimum, but of a higher value (Fig. 7). Therefore, we can infer from these observations that the AW is in some way transported from the Strait of Gibraltar into the core of the WAG. We anticipate now that the geostrophic current obtained, if stationary, cannot be responsible for such transport, which must be across the geostrophic streamfunction.

A consequence of this homogeneous salinity layer is that whereas, say at 100 m, the salinity gradients re-

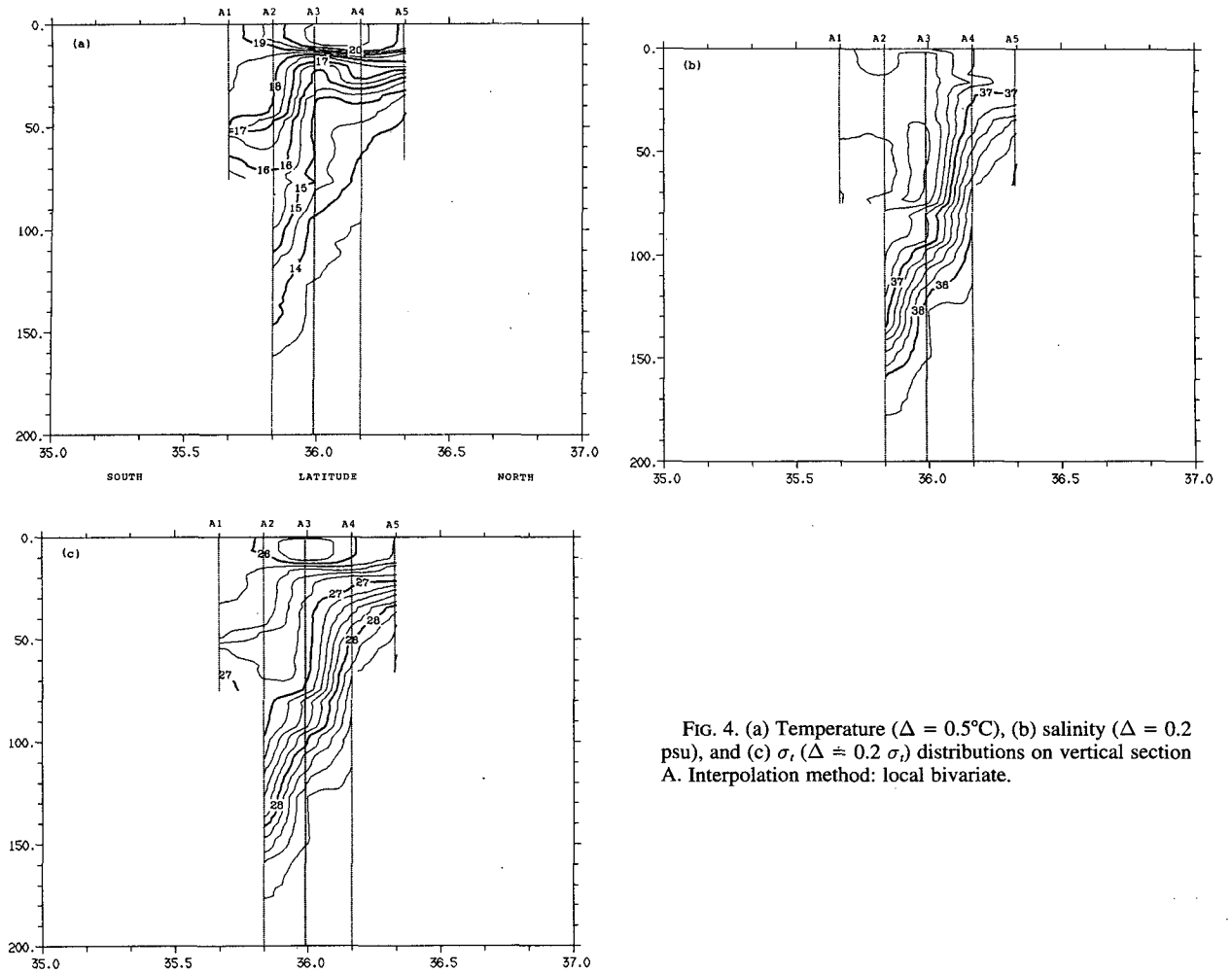

FIG. 4. (a) Temperature (Δ = 0.5°C), (b) salinity (Δ = 0.2 psu), and (c) σ_t ($\Delta \doteq 0.2\ \sigma_t$) distributions on vertical section A. Interpolation method: local bivariate.

produce the wavelike front better than the gyres, the temperature gradients reproduce the WAG better than the front (Fig. 2). To measure the relative importance of each contribution to the density field, we have computed the density distribution at 100 m taking into account only temperature or salinity variations. Figure 8 shows that the temperature gradients at 100 m mainly control the density gradients in the WAG, whereas salinity gradients control the density gradient in the front. The vertical distributions of temperature and salinity in the core of both anticyclonic gyres are quite similar (Fig. 9). Both gyres present a subsurface salinity minimum between 20 and 140 m approximately, but the EAG has higher salinities and lower temperatures, and therefore denser water. Both profiles contrast with the typical vertical distribution north of the front, where a clear thermocline can be observed at about 20–30 m depth.

The vertical extension of the gyres is of the order of 200–220 m, the WAG being deeper (compare 27.0 σ_t surface) and with stronger density gradients (Fig. 3). However, the surface signature is weak. The horizontal temperature distribution at 10 m (Fig. 10) is quite different from the two-gyre system described before and quite similar to the satellite image (Fig. 11) obtained on 28 September 1992. The most relevant feature in this satellite image is the temperature gradient beginning at Cape Tres Forcas and progressing northeastward, being very similar to the in situ surface temperature distribution. This is a track of the front, but the thermal pattern is not closed and therefore the EAG is not observed. The similarity of both pictures in the western Alboran increases if we ignore the cold filament in Fig. 11 extending from the Spanish to the Moroccan coast following a curved path, which is too narrow to be captured by our sampling. Also, the horizontal extension of the gyres (from the African coast to ~36°20′N) is smaller than usually derived from satellite imagery when the gyres reach their maximum width (e.g., Heburn and La Violette 1990).

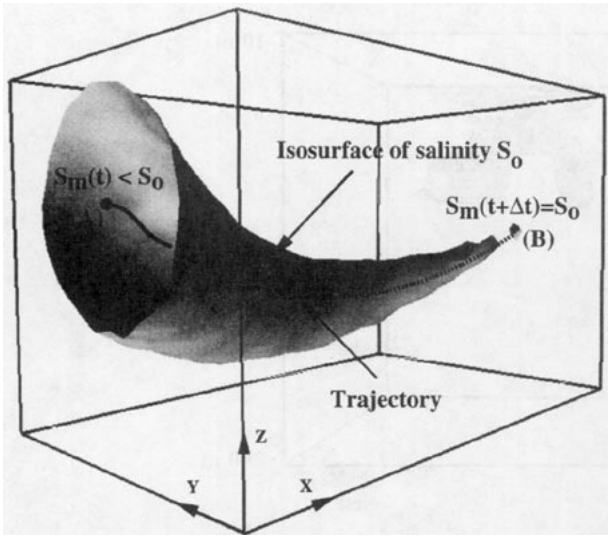

FIG. 5. Sketch to represent how the relative subsurface salinity minimum S_m flowing throughout the Alboran Sea is used as a tracer. Assuming homogeneous mixing the relative salinity minimum does not lose its minimum condition over the trajectory between points (A) and (B).

Between Almería and Oran the front does not acquire the large differences in salinity and temperature that characterize the Almería–Oran density front reported in previous studies (Tintoré et al. 1988; Arnone et al. 1990) but conserves its structure without changes in the gradients. The origin of the Algerian Current can be observed where the front reaches the African coast at about 0°30′W. Some indication of a new, more relaxed, density gradient can be found in the northeastern boundary of the sampled region, but the incomplete sampling prevents further conclusions.

In order to obtain the 3D dynamic topography field, and hence all the dynamic variables, we interpolate the dynamic height data computed at each CTD station onto a regular grid of 9.3 × 6.7 km, the vertical resolution being 1 m. The objective analysis used was a method of successive corrections (SC) using weighting functions normalized in such a way that the result after infinite iterations can be demonstrated to be equivalent to the result of an optimal interpolation (OI) method (Brathset 1986; Franke 1988). The characteristic scale of the weight functions, which plays the role of a correlation function in OI methods, has been estimated by cross validation and has been set equal to 20 km (D. Gomis and M. Pedder 1993, personal communication).

The dynamic topography was computed twice using a reference level of 200 and 300 m, resulting in mean differences in the geostrophic transport between stations of about 10%. The 200–250 m level is the approximate level that separates eastward flowing AW from westward flowing MW and has been used frequently in geostrophic computations (e.g., Lanoix 1974; Perkins et al. 1990). In order to include the crucial dynamic information in the coastal zones where water depth is only 200 m, especially at the African coast, and to compare our results with previous works, we decided to take the reference level at 200 m. The results are summarized in Figs. 12 and 13. The wavelike jet dominates the circulation, coupled with two anticyclonic gyre–cyclonic eddy systems. We will use the geostrophic transport function (Fig. 13) to distinguish unambiguously between the wavelike jet or wavelike front (wavelike isolines) and the gyres (closed isolines). Maximum values of geostrophic velocity are about 1 m s^{-1} in the Atlantic jet north of the WAG. Note that from this geostrophic circulation the core of the gyres are isolated from the jet, and therefore the geostrophic circulation cannot produce the interchange of water between jet and gyres as we previously described for the AW. The ADCP data reproduces a circulation very similar to the geostrophic one, both anticyclonic gyres being well observed (Fig. 14). The ADCP data requires a posterior careful processing, calibration and filtering of tidal and inertial waves, and therefore a limited use is made of this data here. Nevertheless, from Fig. 14 we can observe the clear deviation from geostrophy of the flow at 35°50′N, 5°W. This ageostrophic circulation, pointing southeastward, might be responsible for advecting AW into the core of the WAG.

The geostrophic transport (from 10 to 200 m, Fig. 13) of the wavelike jet is very close to 1 Sv (Sv ≡ 10^6 m^3 s^{-1}), whereas the mean geostrophic transport of the WAG and EAG is 1.6 and 1.2 Sv, respectively. It must be noted that the jet transport (~1 Sv) differs from the input and output transport in the Alboran Sea. The input transport between stations A01 and A03 and the output between stations P10 and P08 (origin of the Algerian Current) is 1.8 Sv. Such variations are due to the recirculation and splitting of the flow that takes place mostly south of the main jet.

The geostrophic relative vorticity field (Fig. 15) shows the importance of several mesoscale phenomena. Negative relative vorticity is associated with the large anticyclonic gyres, values being higher in the WAG where $\zeta = -0.6f \sim -5 \times 10^{-5}$ s^{-1} ($f = 8.57 \times 10^{-5}$ s^{-1} is the planetary vorticity at 36°N), whereas large positive values are due to three mesoscale phenomena (A, B, and C in Fig. 16): (A) the cyclonic eddies, $\zeta = 0.4f \sim +3.5 \times 10^{-5}$ s^{-1}; (B) the curvature change of the jet west of Cape Tres Forcas, $\zeta = 0.4f \sim +3.5 \times 10^{-5}$ s^{-1}; and (C) the strong meridional shear $-\partial u/\partial y$ (located at 36°10′N, 4°30′W) due to the large differences between the speed of the jet (up to 1 m s^{-1}) and the slow waters in the north, $\zeta = 0.6f \sim +5 \times 10^{-5}$ s^{-1}.

Having described the geostrophic velocity and vorticity field, we close this section with some results con-

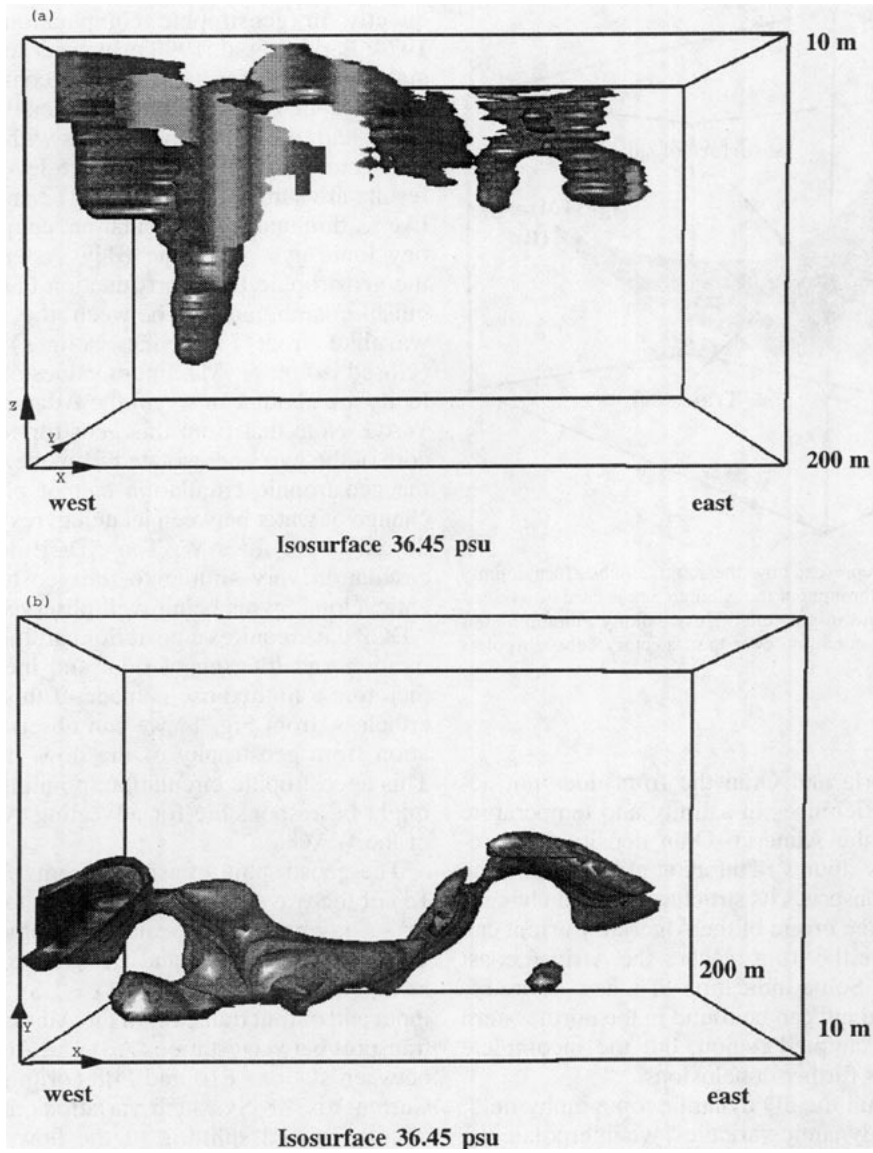

FIG. 6. Isosurface of 36.45 psu: (a) top view, (b) lateral view. The box is that represented in Fig. 1. The z spacing between data points is 1 m. The lateral boundary represents the surface limited by the external CTD stations, and not the coastal boundary.

cerning static and baroclinic stability. Brunt–Väisälä frequency profiles were computed from the 1-m spaced density data using the adiabatic leveling method (Bray and Fofonoff 1981; Millard et al. 1990). The vertical stratification during the cruise (September–October) presents a clear horizontal anisotropy (Fig. 17). The largest values of squared Brunt–Väisälä frequency N^2 (200–300 cycles^2/hour^2) are located at ~30-m depth. Such large values due to vertical temperature differences characterize the thermocline, which is present north of the wavelike front, where the currents are very weak. Relative maximum values of N^2 [50–100 (cph)^2, in the western Alboran] extend down (Fig. 18) following the tilt of the density field to the bottom of both gyres (~150 m) where the stratification becomes greater [$100 < N^2 < 140$ (cph)^2 in the WAG, and $60 < N^2 < 100$ (cph)^2 in the EAG].

The distribution of the vertical shear $U_z^2 + V_z^2$ at 100 m is shown in Fig. 19. Isolines of vertical shear follow the wavelike jet reaching absolute maximum values north of the WAG and relative maxima at the changes of flow curvature (crests and troughs). Flows with

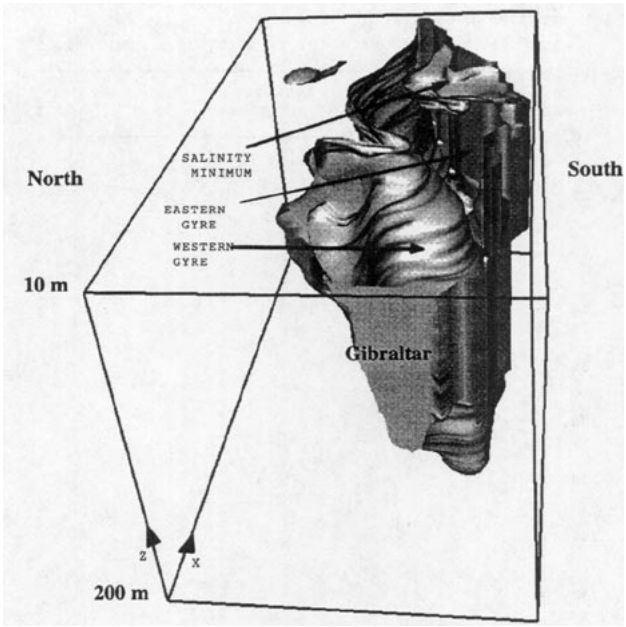

FIG. 7. Isosurface of 36.7 psu. Western and eastern Alboran gyres are referenced. The box is that represented in Fig. 1. The z spacing between data points is 1 m.

strong velocity shears may be unstable with respect to small perturbations. Baroclinic instability depends primarily on vertical shear in the jet stream, and therefore, the north of the WAG might be a place for baroclinic instability processes.

4. Potential vorticity

For adiabatic, frictionless motion, Ertel's potential vorticity (PV)

$$q = \rho^{-1}(2\Omega + \nabla \times \mathbf{u})\cdot\nabla\rho \qquad (1)$$

is conserved following a particle. Here Ω is the earth's angular velocity, $\mathbf{u}$ is the water velocity relative to the earth, and ρ is the water density. Therefore, if dissipative effects and diabatic processes are insignificant, q is a conservative property and under these conditions it can be used as a tracer of the circulation.

We follow Pollard and Regier (1992) in using the hydrostatic approximation and f-plane geometry, reducing (1) to

$$q = -fg^{-1}N^2(1 + \zeta f^{-1} - F), \qquad (2)$$

where N^2 is the Brunt–Väisälä frequency, ζ is the geostrophic relative vorticity, $F = (U_z^2 + V_z^2)/N^2$ is the Froude number, and (U, V) is the geostrophic velocity. The terms on the right-hand side of (2) represent contributions to q from the planetary vorticity, the (vertical component of) geostrophic relative vorticity, and the horizontal components of geostrophic relative vorticity, respectively.

In this section we investigate the importance of stratification, relative vorticity, and Froude number in the PV distributions and show how this gives us an order of magnitude of the associated vertical motion. We will concentrate on the baroclinic jet and WAG between stations D04, D07, E04, and E07 because the flow is approximately zonal reaching the maximum velocities and strongest shears, and because the temporal scale of the motion (the time required for the flow to travel from vertical section D to E at 100 m is less than one day) justifies the assumption of adiabatic motion in the PV conservation. Therefore, from the regular 3D matrix horizontally interpolated (vertical spacing of 1 m) we extract the vertical cross sections closest to the vertical sections D and E. Since the maximum distance between the interpolated and the original meridional vertical sections is less than 5 km (half of the x spacing), we will denote these interpolated vertical sections also as D and E. The different terms in (2) are shown in Fig.

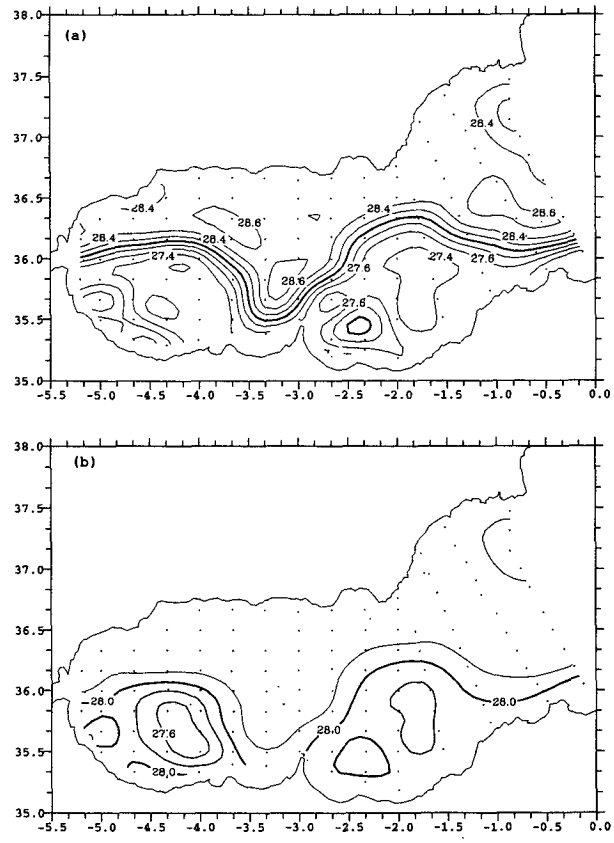

FIG. 8. The density field ($\Delta = 0.2\ \sigma_t$) at 100 m (a) due to the observed salinity field and the mean temperature on this layer (14.2°C) and (b) due to the observed temperature field and the mean salinity on this layer (37.6 psu). Interpolation method: successive corrections.

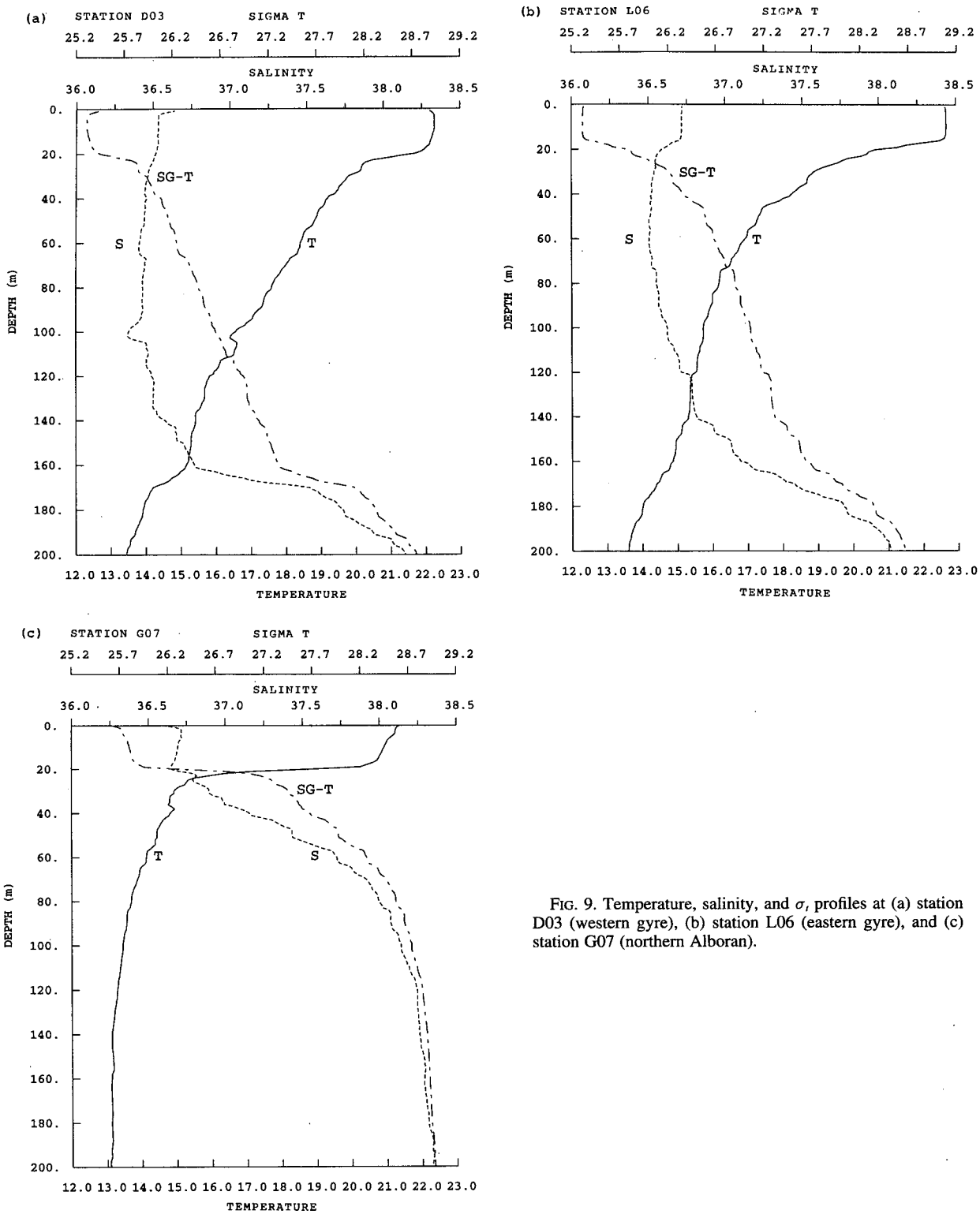

FIG. 9. Temperature, salinity, and σ_t profiles at (a) station D03 (western gyre), (b) station L06 (eastern gyre), and (c) station G07 (northern Alboran).

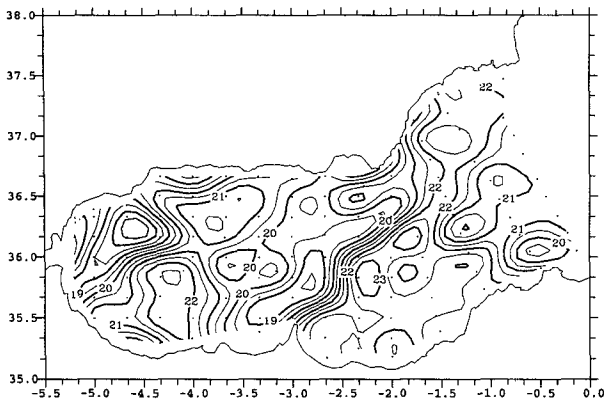

FIG. 10. Temperature distribution at 10 m (Δ = 0.5°C). Interpolation method: successive corrections.

20. The zone of interest (bounded by a box in those panels) extends from 60 m (below the thermocline) to 140 m, including the eastward jet as well as the northern circulation of the WAG. Note that this box is below the effects of surface-layer mixing.

In order to understand the several terms in (2) we show first the density distributions (Fig. 20a). Thickness increases with depth between isopycnals greater than ~28.4 σ_t in vertical section D and greater than ~28.2 σ_t in vertical section E (left side of the box); thickness is more or less constant over these isopycnals and decreases for smaller density values (right side of the box), and as a result, as we commented in section 3, high stratification values extend down from the thermocline to the bottom of the WAG. Moreover, the thickness in vertical section E is smaller in relation to vertical section D.

The vertical distributions of N^2 (Fig. 20b) shows the significant increase of stratification in the area bounded by the box between vertical sections D and E. Typical values in the box are 25–30 $(\text{cph})^2$ in vertical section D and 50–100 $(\text{cph})^2$ in vertical section E. Observe also the smoothed field in section E in relation with Fig. 18 due to the differences between horizontal OI and vertical local bivariate interpolation method.

The zonal geostrophic velocity distribution (Fig. 20c) for vertical section D shows the strong eastward flow reaching maximum velocities of 100 cm s^{-1} at depth 10 m. The zonal geostrophic velocity is close to zero in the core of the WAG, while the westward flow (corresponding to the southern WAG) reaches maximum values of ~60 cm s^{-1}. The eastward flow slows in vertical section E (maximum velocities of 60 cm s^{-1}) at the same time that it becomes wider (from stations E3 to E8). The speed of the flow in the box decreases by about 20 cm s^{-1}, whereas the westward flow remains very similar in both vertical sections.

The relative vorticity distribution ζ/f (Fig. 20d) in vertical section D presents a clear separation between positive and negative values. The eastward flow is divided into two symmetric parts: a cyclonic (corresponding mainly to the wavelike jet) and an anticyclonic part (corresponding mainly to the WAG). This is because the positive relative vorticity of the wavelike jet between stations D5 and D6 is produced by meridional shear (the curvature of the jet being small here). This separation occurs approximately in the middle be-

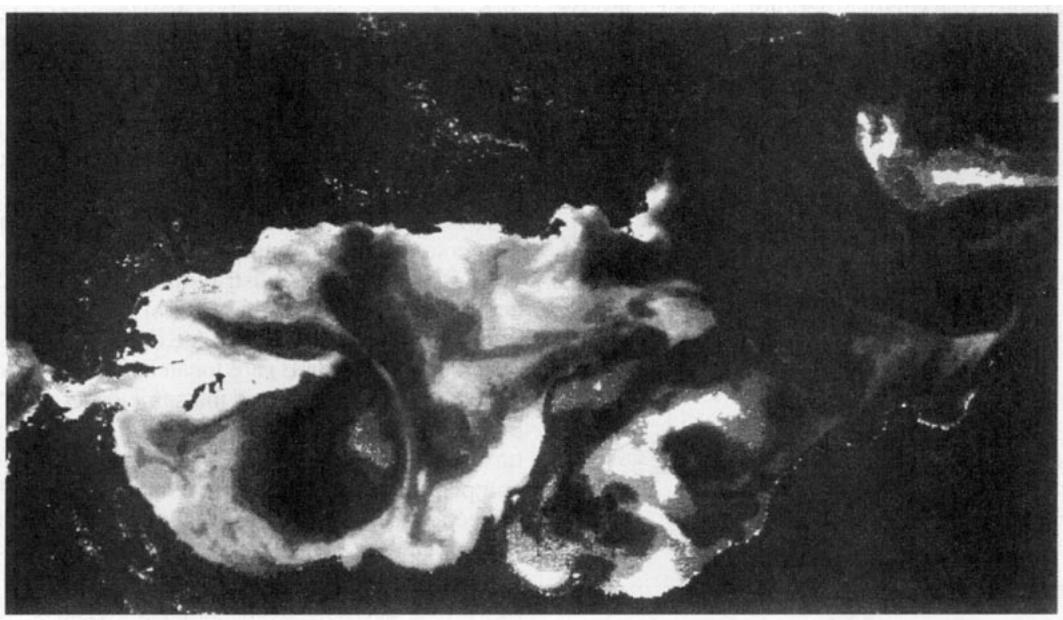

FIG. 11. Satellite thermal imagery (28 Sep 1992). Light color means colder water.

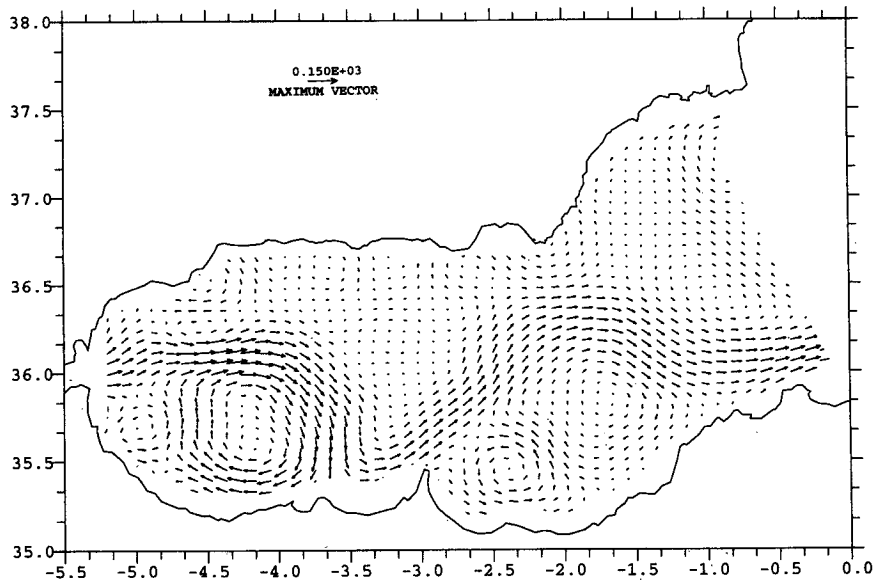

FIG. 12. Geostrophic velocity field at 10 m. Reference vector is 1.5 m s^{-1}.

tween stations D5 and D6. The WAG has two vertical regions of high relative vorticity separated by a region of smaller relative vorticity in the center of the gyre where the horizontal velocity is uniform near zero (Fig. 20c). Maximum relative vorticity values are about $\pm 0.6f$ in the first 30 m and typical values of $\pm 0.3f$ in the box in vertical section D. Vertical section E shows quite a different picture. Although the relative vorticity in the southern part of the WAG is similar, the relative vorticity corresponding to the eastward flow has decreased to $0.1f$ (a decrease of 50% in relation with section D) due to the smaller meridional shear. Observe also the vertical tilting of ζ isolines produced by the vertical tilting in the zonal geostrophic velocities.

The geostrophic vertical shear $U_z^2 + V_z^2$ (Fig. 20e) reaches maximum values in the eastward flow of 50 $\times 10^{-6}$ s^{-2} at ~120 m in section D, and 40 $\times 10^{-6}$ s^{-2} in section E. Note how the strong vertical shear is confined to a narrow area between stations D4 and D7 (due to the vertically oriented frontal surface), while the vertical shear in section E occupies a wider area. This is a result of the different slope of maximum density gradient with respect to depth in vertical sections D and E. Vertical section D presents a vertically oriented frontal area between stations D4 and D7, while vertical section E presents a sloping of the frontal zone (this is also clearly observed from the zonal geostrophic velocity distributions in Fig. 20c). It is well known (e.g., Holton 1979, p. 242) that a stationary frontal zone must slope with depth: a vertically oriented frontal surface is not a baroclinically stable configuration. It follows that the configuration of the eastward jet is baroclinally more stable in vertical section E than in vertical section D.

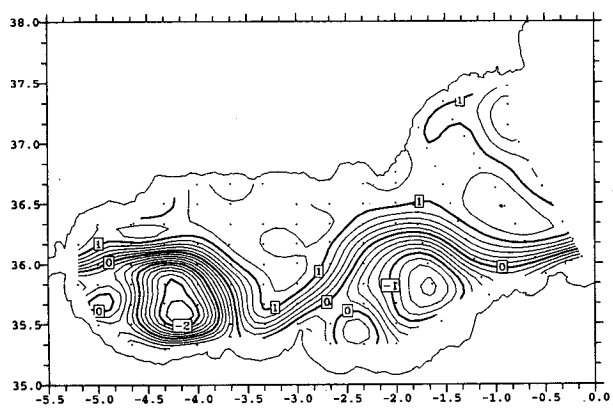

FIG. 13. Geostrophic transport function at 10 m (Δ = 0.2 Sv).

A decrease in the Froude number $(U_z^2 + V_z^2)/N^2$ in (2), along with conservation of q, suggest a possible conversion of horizontal relative vorticity to vertical vorticity. The vertical distributions of F (Fig. 20f) can be explain in terms of the vertical shear and stratification. Large values of the Froude number (0.4 in section D and 0.2 in section E) are located in the eastward flow at about 100 m and are of the same order as ζ/f in the box. Both distributions exhibits a similar vertical structure (the vertical tilt of vertical shear in section E is compensated by the tilt of stratification), but F values in section E have decreased about 50% in relation to section D.

The resulting PV distribution is shown in Fig. 20g. In vertical sections D and E large negative values of relative vorticity dominate the PV distribution altering

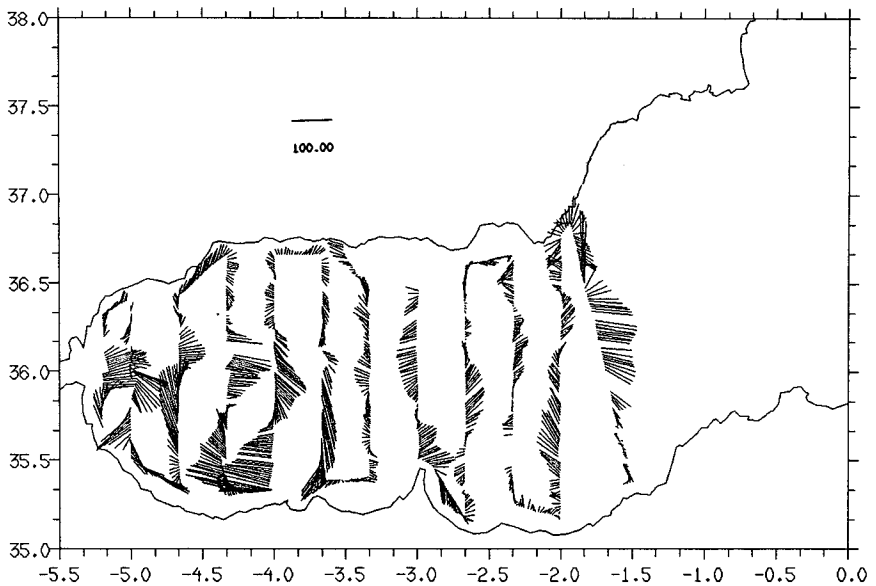

FIG. 14. ADCP data at 40-m depth. Reference vector is 1 m s^{-1}.

the PV field produced by the rather uniform horizontal distributions of stratification from the surface to ~80 m (places A, B, and C in Fig. 20g). In the left side of the box in section D negative relative vorticity and large Froude number combine to reduce the absolute PV, whereas in the right side positive relative vorticity and large Froude number compensate each other increasing absolute PV. In section E, however, the combined effects of relative vorticity and Froude number are small compared to 1, and therefore the PV distribution is very similar to the N^2 distribution. Comparing both PV fields in the upper part of the two boxes, we can observe how PV has been transported from box D into box E smoothing the PV gradients between surface (eastward jet) and deep (bottom of the WAG) PV distributions. A series of plots (for vertical section D, for the vertical section in the middle of D and E, and for section E) of PV and density distributions in the box is shown in Fig. 21. The three small areas represent three particles of fluid limited by the same density and PV values, labeled A, B, and C. From vertical section D to E we can observe how particles move southward (to the left side of the box); particles A and B have a downward motion, while particle C is more static. Therefore we can infer that, between vertical sections D and E, besides the southward advection due to the small horizontal curvature of the flow, downward motion must take place in the middle of the box, with a zone of zero vertical motion to its right. An order of magnitude of this vertical motion can be given if local changes in the PV are neglected. In this case the vertical motion of a zonal flow implies

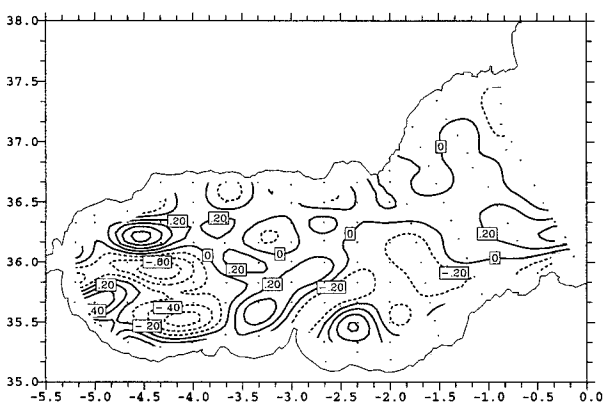

FIG. 15. Geostrophic vorticity field, ζ / f, at 10 m (Δ = 0.2).

$$(u, w)\cdot\left(\frac{\partial q}{\partial x}, \frac{\partial q}{\partial z}\right) = 0. \tag{3}$$

Since the trajectory of the fluid particle must be on a q-surface,

$$dq = \frac{\partial q}{\partial x}\,dx + \frac{\partial q}{\partial z}\,dz = 0$$

over the trajectory, and from (3), on a q-surface, and in finite-difference form

$$w = -\,u\left(\frac{\partial q/\partial x}{\partial q/\partial z}\right) = u\,\frac{\Delta Z}{\Delta X}, \tag{4}$$

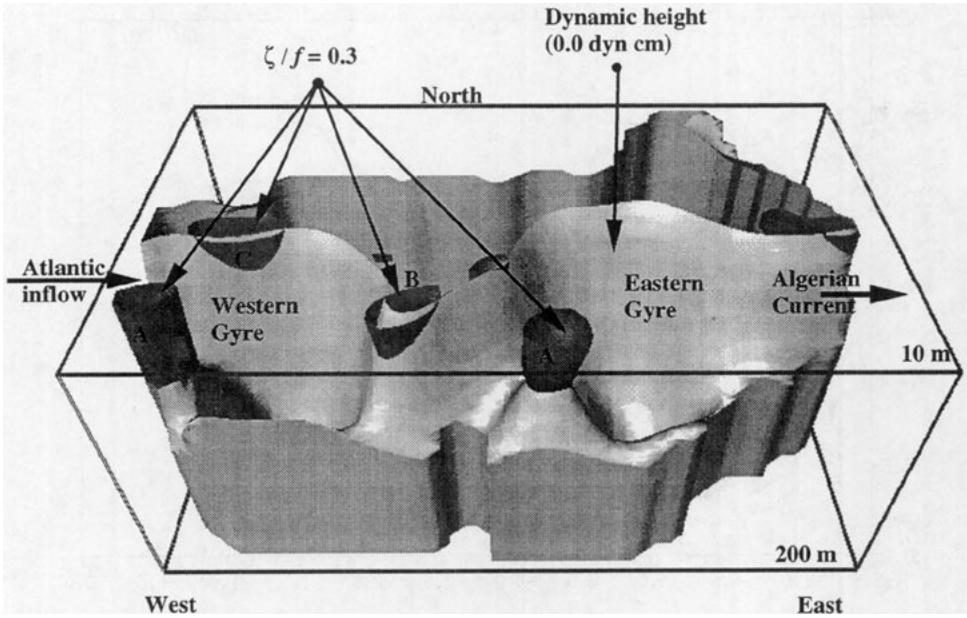

FIG. 16. Isosurface of positive geostrophic vorticity ($\zeta = 0.3f$). The isosurface of dynamic height of 0 dyn cm is ploted just to locate the wavelike flow. The z spacing between data points is 1 m.

where ΔZ and ΔX are the spatial increments in the particle trajectory. Since the trajectory of the three fluid particles has been previously obtained, we can compute the order of magnitude of their vertical motion. Using $u = 0.4$ m s^{-1}, the mean eastward (along front) horizontal geostrophic velocity at 80 m, $\Delta X = 30$ km, the distance between interpolated vertical sections, and $\Delta Z = -10$ m the vertical displacement, then $w = \Delta Z \times u/\Delta X \sim -10 \times 10^{-5}$ m s^{-1}.

5. Vertical velocity from QG theory

Vertical velocities on wavelike circulations have been obtained in several previous works, most notably with Gulf Stream meanders (Chew et al. 1985; Bower 1989). Usually the results agree well with the theory of baroclinic waves, which predicts that upward vertical motion takes place upstream (downstream) of the crest (trough) and downward vertical motion takes place downstream (upstream) of the crest (trough)

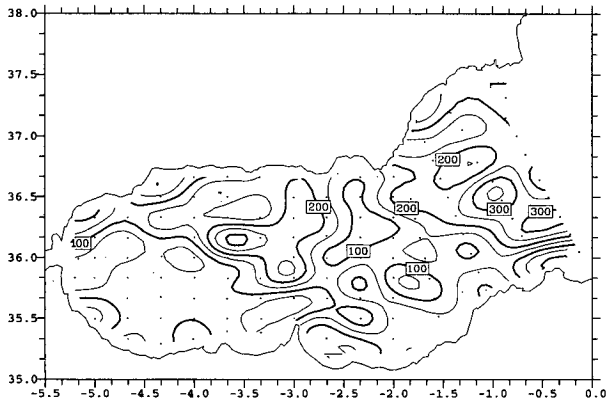

FIG. 17. Distribution of the squared Brunt–Väisälä frequency at 30 m [$\Delta = 50$ (cph)^2]. Interpolation method: sucessive corrections.

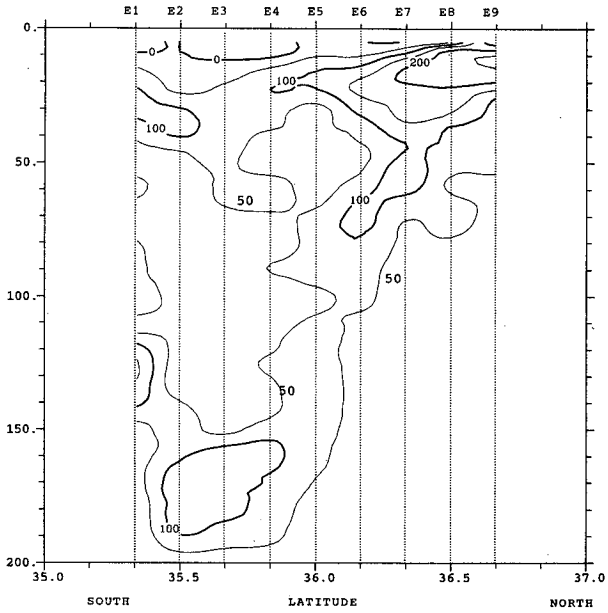

FIG. 18. Squared Brunt–Väisälä frequency on vertical section E [$\Delta = 50$ (cph)^2]. Interpolation method: local bivariate.

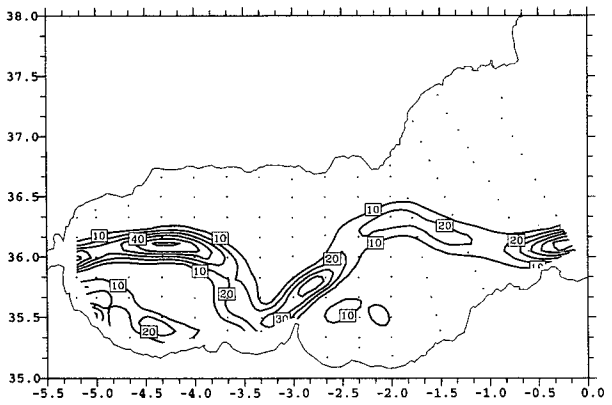

FIG. 19. Distribution of vertical shear $U_z^2 + V_z^2$ at 100 m ($\Delta = 10 \times 10^{-6}$ s^{-2}).

(e.g., Palmen and Newton 1969, p. 144; Holton 1979, p. 136). In this situation the differential vorticity advection term in the omega equation (e.g., see Holton 1979, p. 136) plays the main role in forcing the vertical velocities. In the Alboran Sea the vorticity field is modified by the presence of the inflow at the Strait of Gibraltar (which produces strong horizontal shears) and by the presence of coastal boundaries. Furthermore, mesoscale processes (eddies and meanders along the jet) distort the typical vorticity field of an unbounded wavelike circulation. For example, Tintoré et al. (1991) found that vertical velocities due to mesoscale phenomena are an order of magnitude larger than the vertical motion associated with the large-scale gyres. In Viúdez et al. (1996a, hereinafter Part II) it is shown that although the differential vorticity advections dominate the forcing in some areas of the western basin, it is does not fully explain the forcing of QG vertical velocities in the Alboran Sea: consideration of the Laplacian of the density advection is also required.

A derivation of the generalized omega equation without cancellation of terms on the f plane, without heating and friction, is given in the appendix (see also the appendix for the definition of the symbols used). Equation (A4) establishes that in quasigeostrophic theory, on the f plane, the vertical velocity is forced solely by the divergence of $\mathbf{Q}$. Furthermore, if ageostrophic motion is neglected in the thermodynamic equation, then

$$\left(\frac{\partial}{\partial t} + \mathbf{V}\cdot\nabla\right)\nabla\rho = \frac{-\rho_0 f}{g}\mathbf{Q}, \qquad (5)$$

and $\mathbf{Q}$ is proportional to the time rate of change of the density gradient moving with the horizontal geostrophic velocity (Hoskins et al. 1978). The $\mathbf{Q}$ field at 100 m is shown in Fig. 22. In the northwestern part of the WAG (36°00′N, 4°30′W) $-\mathbf{Q}$ vectors point northward ($\mathbf{Q}$ southward) in a similar direction to the horizontal density gradient. Therefore, the fluid particles following geostrophic motion in this region tend to increase their horizontal density gradient (as a result, the geostrophic transport function indicates a zone of confluence, Fig. 13). On the other hand, in the northeastern part of the WAG (36°00′N, 4°00′W) $-\mathbf{Q}$ vectors point southward ($\mathbf{Q}$ northward) in a direction opposite to the horizontal density gradient, and therefore the fluid particles must have a tendency to decrease their horizontal density gradient (as a result, the geostrophic transport function indicates a zone of diffluence). Similar features can be observed in the south of the WAG and north of the EAG and a confluent zone at the beginning of the Algerian Current. The north of the gyres, therefore, can be associated with zones of frontogenesis. The $\nabla\cdot\mathbf{Q}$ term was computed directly from the gridded dynamic height field $\Psi(x, y, z)$ (see Part II for a statistical comparison using another ways to compute $\nabla\cdot\mathbf{Q}$). The $\Psi(x, y, z)$ field itself was computed in two ways: Method (A) it was obtained by interpolation (SC) from the values of $\Psi_i(z)$ at stations and method (B) [due to the results obtained in Part II using a primitive equation (PE) model] from the already interpolated (SC) density field $\rho(x, y, z)$. The results indicated that, in a few specific areas, differences were of second order in, for example, the advection of geostrophic vorticity, but of first order in its vertical derivative. Method (B) gave better results (in comparison with the PE results) and therefore was used here to compute $\mathbf{Q}$ and $\nabla\cdot\mathbf{Q}$.

The $\nabla\cdot\mathbf{Q}$ term was therefore computed at each grid point using central differences directly from the dynamic topography field (in such a way that a maximum of five grid points in each horizontal axis was required) using the expanded expression [here written in terms of geostrophic velocities (U, V)]

$$\nabla\cdot\mathbf{Q} = -U_{xx}V_z - U_xV_{xz} + V_{xx}U_z + V_xU_{xz} - U_{yy}V_z - U_yV_{yz} + V_{yy}U_z + V_yU_{yz},$$

and the contribution of each term was analyzed. The results showed that $U_{yy}V_z$ (meridional change of meridional shear U_y times vertical shear V_z) is dominant. The empirical error in the term $U_{yy}V_z$ at 100 m can be roughly estimated assuming a random error in the density data from 200 to 100 m to be $\epsilon_\rho = 10^{-2}$ kg m^{-3}. Using a trapezoidal rule of integration to obtain the dynamic height from specific volume anomalies, the error in the geostrophic velocity U, obtained from a second-order derivative (e.g., Atkinson 1988, p. 319), is $\epsilon_U(100\text{ m}) \sim (1/3) \times 10^{-2}$ m s^{-1}, which implies $\epsilon_{U_{yy}} = 4\epsilon_{U_y}/\Delta y^2 \sim (1/4) \times 10^{-9}$ m^{-1} s^{-1}. The error in V_z can be obtained from the "thermal wind" relation (A2) $\epsilon_{V_z} = g\epsilon_\rho/(f\rho\Delta x) \sim (1/8) \times 10^{-3}$ s^{-1}. Finally, $\epsilon_{U_{yy}V_z} \sim [(\epsilon_{U_{yy}}V_z)^2 + (U_{yy}\epsilon_{V_z})^2]^{1/2} \sim 12 \times 10^{-13}$ m^{-1} s^{-2} for high values of V_z (5×10^{-3} s^{-1}) and U_{yy} (10^{-9} m^{-1} s^{-1}), resulting $2f\,\epsilon_{U_{yy}V_z} \sim 20 \times 10^{-17}$ m^{-1} s^{-3},

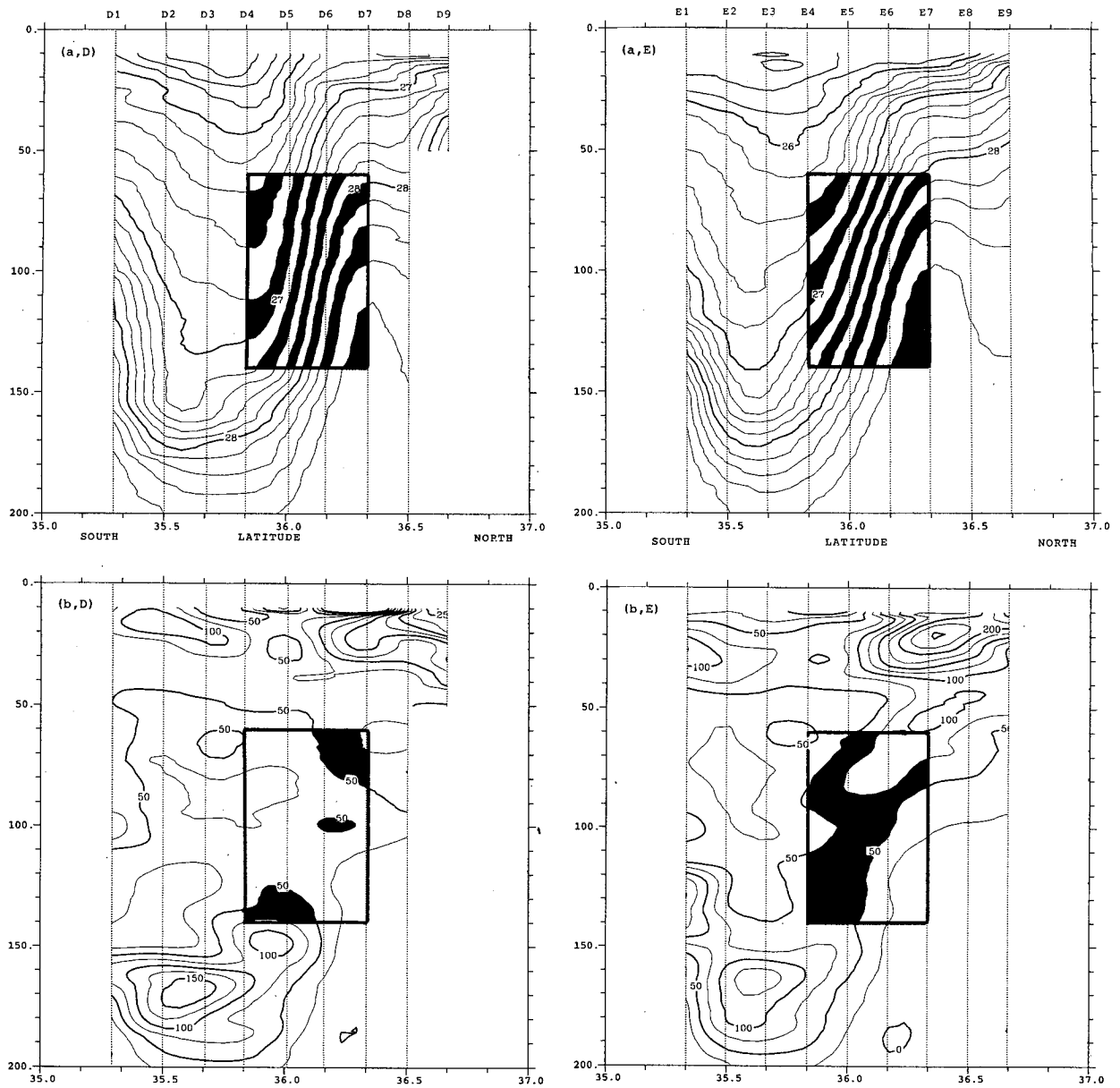

FIG. 20. Vertical distributions in vertical section D and E of (a) σ_t ($\Delta = 02\sigma_t$), (b) squared Brunt–Väisälä frequency [$\Delta = 25$ (cph)^2],

which implies an error of 30% in the forcing of the QG omega equation.

Divergence of **Q** at 100 m (Fig. 24) can be identified from the **Q** field (Fig. 22). Divergence of the tendency of the density gradient of the fluid following geostrophic motion takes place mainly in the northern and southern part of the WAG. In the classical quasigeostrophic formulation of the omega equation the forcing is discussed in terms of geostrophic differential relative vorticity advection and the Laplacian of density advection. A drawback of this interpretation is that the two expressions are not fully independent: there exists a high degree of cancellation and addition between both terms. The result is that, in practice, it is very difficult to isolate the two effects. The term $2f^{-1}\Psi_{yyy}\Psi_{xz}$, which is ones of the more important one in our computations, is a contribution from the term

$$-f\,\frac{\partial U_y}{\partial y}\,\frac{\partial V}{\partial z}$$

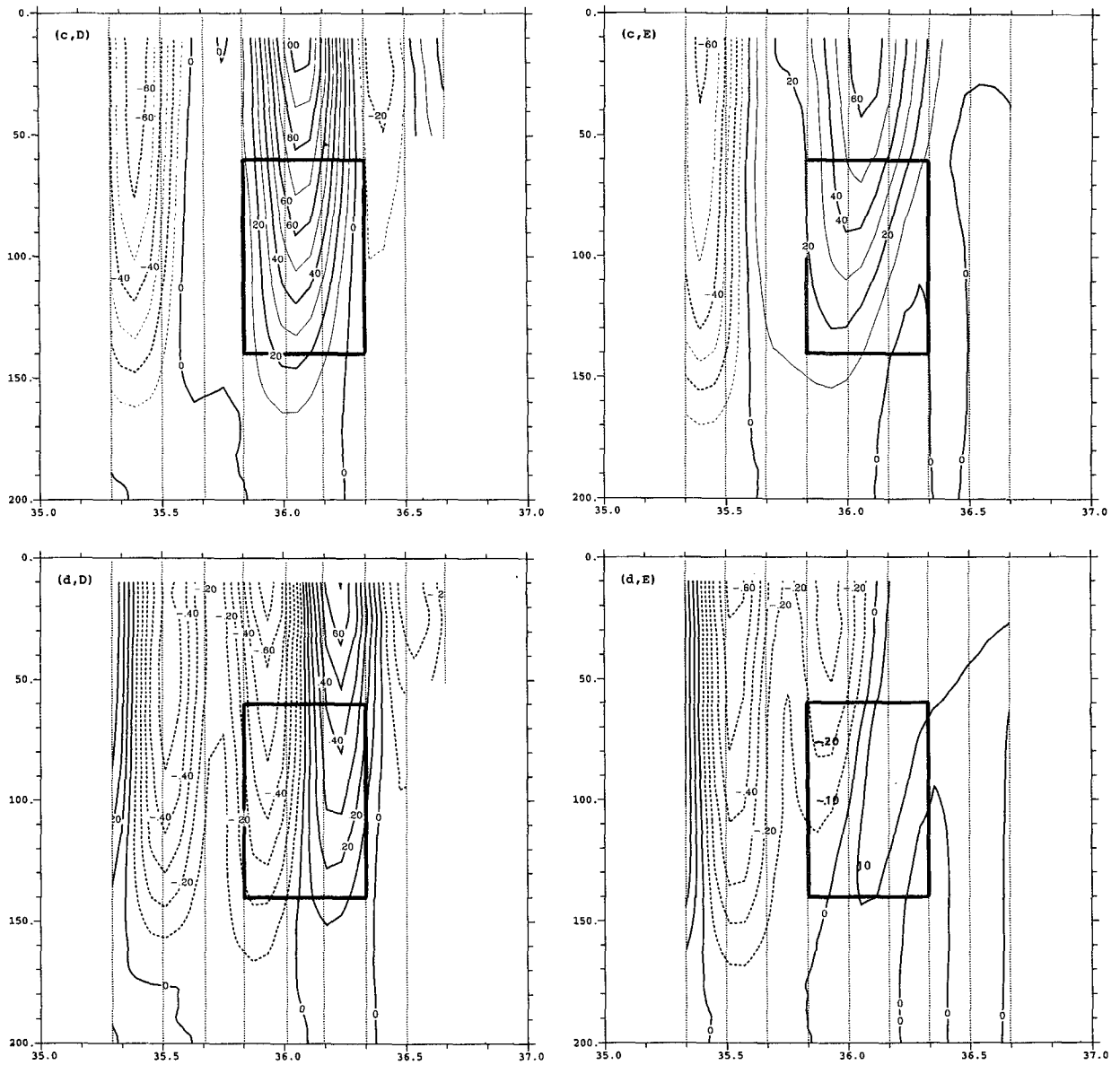

FIG. 20. (*Continued*) (c) zonal component of the geostrophic velocity field (Δ = 10 cm s^{-1}, solid contour lines indicate eastward direction), (d) relative geostrophic vorticity ζ / f (Δ = 0.1),

in the differential vorticity advection and from the term

$$g\rho_0^{-1}\frac{\partial^2 U}{\partial y^2}\frac{\partial \rho}{\partial x}$$

in the Laplacian of density advection. Another important term is $-2f^{-1}\Psi_{yyx}\Psi_{yz}$ (which comes from

$$-f\frac{\partial U_y}{\partial x}\frac{\partial U}{\partial z}$$

in the differential vorticity advection and from

$$g\rho_0^{-1}\frac{\partial^2 V}{\partial y^2}\frac{\partial \rho}{\partial y}$$

in the Laplacian of the density advection). Since the magnitude of relative vorticity advection usually increases with z (z positive upward), rising motion occurs in areas of positive vorticity advection and downward motion in areas of negative vorticity advection. It is observed that west of Cape Tres Forcas, at 35°30′N,

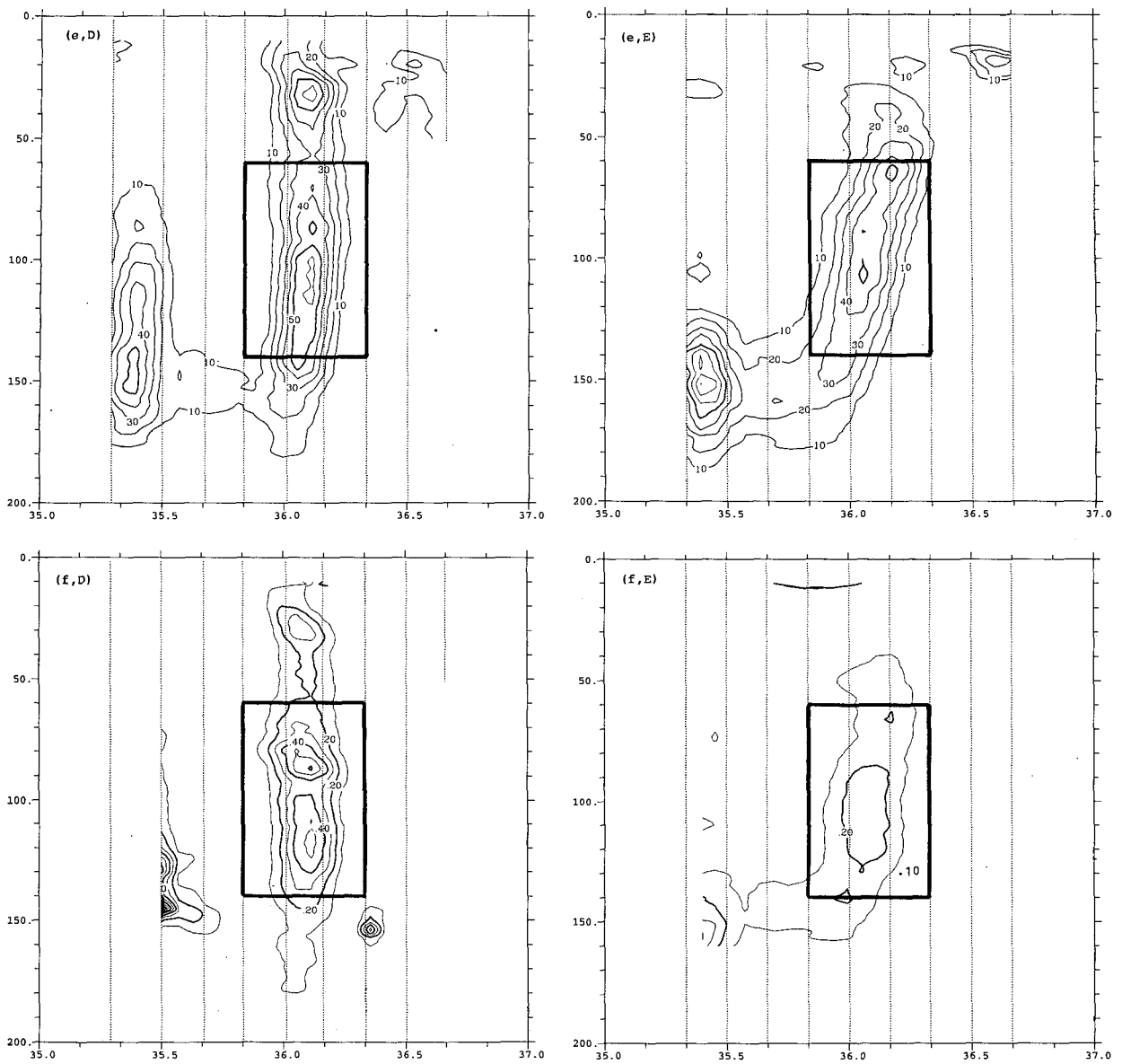

FIG. 20. (*Continued*) (e) geostrophic vertical shear $U_z^2 + V_z^2$ ($\Delta = 10 \times 10^{-6}$ s^{-2}), (f) Froude number $(U_z^2 + V_z^2)/N^2$ ($\Delta = 0.1$), and

3°20′W where the direction of the flow changes quickly, there is a negative advection of relative vorticity ($-\mathbf{V} \cdot \nabla\zeta < 0$) in the western part and positive advection of relative vorticity ($-\mathbf{V} \cdot \nabla\zeta > 0$) in the eastern part, which implies downward and upward motion respectively (see Part II for a detailed explanation of the pattern of QG vertical motion in the western basin). The presence of the coast, however, can make these results questionable because of the limitation of QG theory in the presence of steep topography.

The omega equations (A4) and (A5) were solved with a vertical spacing of 4 m by a direct matrix inversion method based on the algorithm SYMMLQ (Paige and Saunders 1975), which solves the equations by an algorithm based upon the Lanczos process. Sensitivity tests showed that no significant differences in the absolute values of vertical velocities were caused by the use of $N^2(x, y, z)$ or $\bar{N}^2(z)$ (Fig. 23) distributions, and the horizontal pattern of w (zones of upward and downward motion) remained unchanged (see Part II for a series of numerical experiments including random errors). As boundary conditions, we imposed zero vertical velocity in the top, bottom, and lateral boundaries. Using $\partial w/\partial z = 0$ at the bottom did not change the results significally.

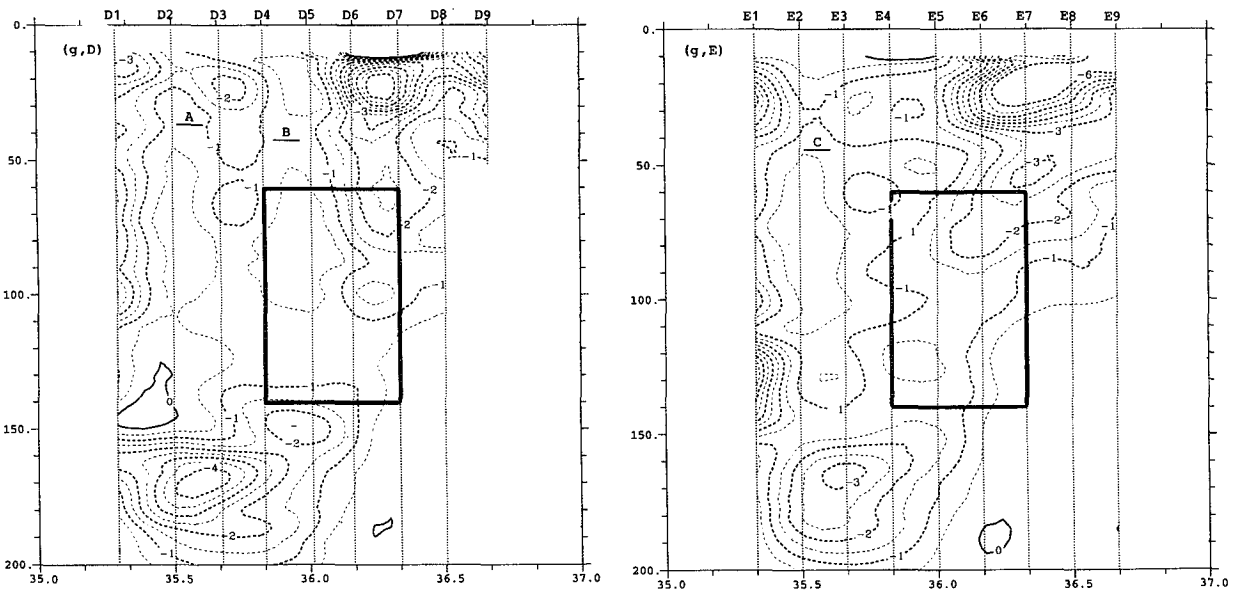

FIG. 20. (*Continued*) (g) potential vorticity ($\Delta = 0.5 \times 10^{-9}$ m^{-1} s^{-1}).

The distribution of the w field at 100 m is shown in Fig. 25. This distribution is closely related to the $\nabla \cdot \mathbf{Q}$ distribution already noted. Maximum significant values of $|w|$ are 15–20 ($\times 10^{-5}$ m s^{-1}).

The vertical distribution of w in a south–north vertical section between vertical sections D and E (corresponding to the section in Fig. 21b) is shown in Fig. 26. Downward motion occurs in the wavelike front (at 36°N) and upward motion in the north (at 36°15′N). Such motion agrees with that inferred from the PV and σ_t conservation.

6. Discussion

The quasigeostrophic vertical velocity field associated with a wavelike front coupled with two large an-

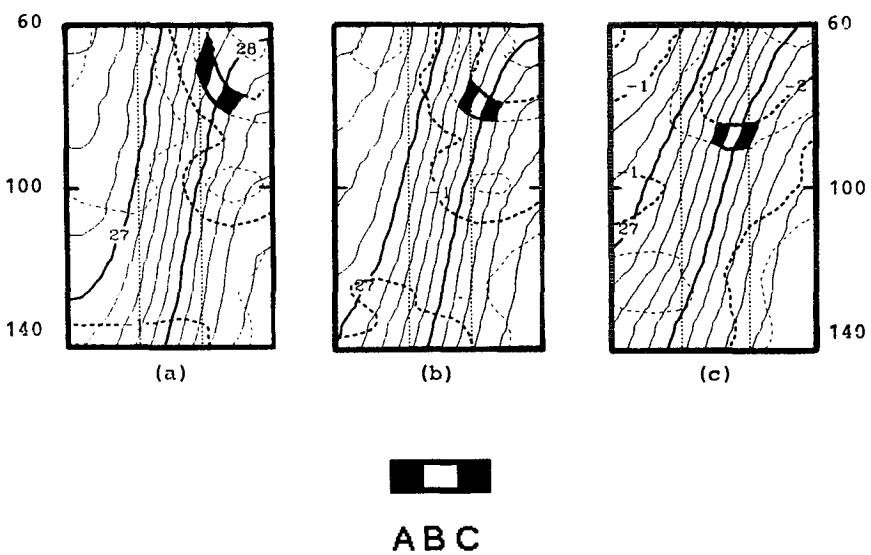

FIG. 21. Vertical distributions of PV ($\Delta = 0.5 \times 10^{-9}$ m^{-1} s^{-1}) and σ_t ($\Delta = 0.2\ \sigma_t$) in the box for (a) vertical section D, (b) vertical section between D and E, and (c) vertical section E. The three small marked areas represent particles of fluid limited by the same values of PV and σ_t.

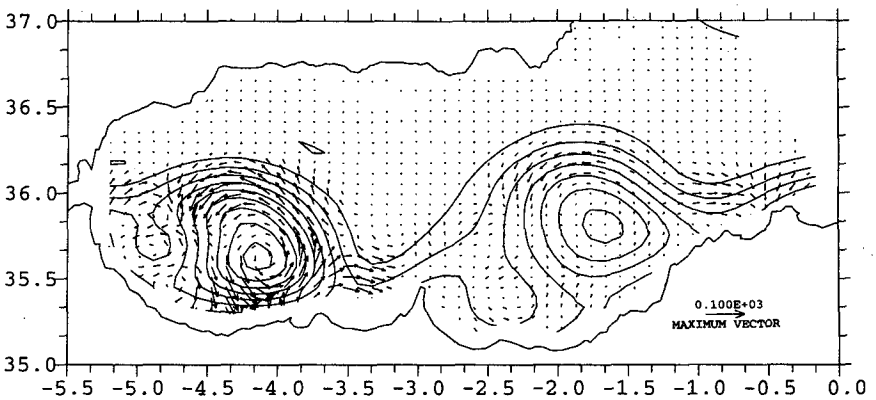

FIG. 22. **Q** vector at 100 m. Reference vector is 100×10^{-9} s^{-2}.

ticyclonic gyre–small cyclonic eddy systems has been obtained. Maximum significant values of quasigeostrophic vertical velocity of 15–20 ($\times 10^{-5}$ m s^{-1}) correspond mainly to mesoscale features in the western Alboran Sea (especially the mesoscale meanders in the WAG, the western mesoscale cyclonic eddy, and the change of curvature of the jet west of Cape Tres Forcas). This order of magnitude agrees with PV conservation along isopycnals. Relative vorticity and Froude number variations were important in the deduction of vertical motion from PV conservation. This agrees with the importance of changes in both horizontal and vertical components of vorticity in the forcing of quasigeostrophic vertical velocities in the omega equation. [It should be noted that relative vorticity has been neglected in the divergence term, $(\zeta_T + f)w_{zz}$ in (A3), but relative vorticity advection terms are included in the forcing $\nabla \cdot \mathbf{Q}$ term.] In relation with the vertical velocities obtained in the *box* in vertical sections D and E it should be noted that, though w is $\sim 10 \times 10^{-5}$ m s^{-1} $\sim$ 10 m d^{-1}, the horizontal currents are also large and therefore the vertical displacements are only about 10 m. The vertical displacements are larger in other areas, for example, west of Cape Tres Forcas, in the cyclonic eddies, or also in the northeast of the WAG (36°N, 3°30′W) where $w < 5 \times 10^{-5}$ m s^{-1} but the horizontal currents are small. Such upwelling in the north of the WAG would be an explanation of the cold narrow filaments observed in satellite imagery. Upwelled cold waters are then advected into the wavelike circulation and are useful tracers of the motion.

A potentially important criticism of our results concerns the synopticity of the analyzed fields. Heburn and La Violette (1990) showed from satellite imagery that the disappearance of either gyre occurs on a timescale of one to two weeks. Nevertheless in our satellite imagery (from 19 Sep to 4 Oct 1992) the large-scale pattern was similar, indicating that at least the WAG was always present.

The Alboran Sea remains one with complex dynamics. Perhaps one of the most important problems concerns the development and maintenance of the gyres.

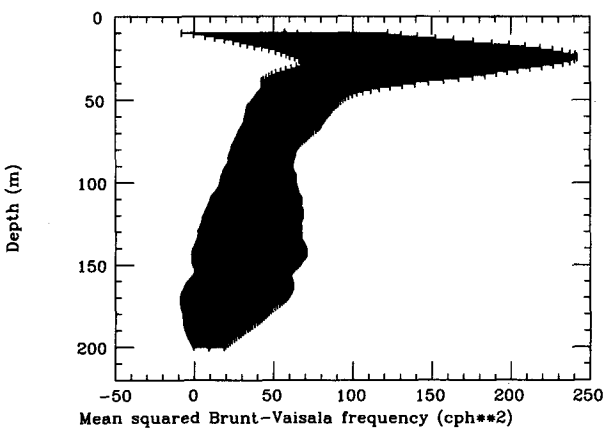

FIG. 23. Mean squared Brunt–Väisälä frequency profile [(cph)^2]. Horizontal bars represent the value $\bar{N}^2(z) \pm$ one standard deviation.

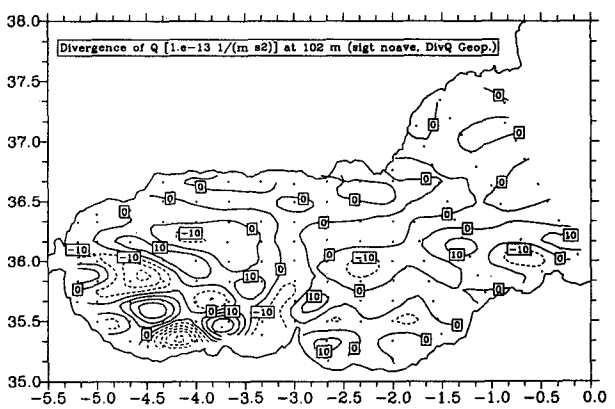

FIG. 24. $\nabla \cdot \mathbf{Q}$ distribution at 100 m ($\Delta = 20 \times 10^{-13}$ m^{-1} s^{-2}).

That the disappearance of the gyres does not have a regular period makes it very difficult to infer the causes, although some correlation has been found between atmospheric forcing and the disappearance of the gyres (Heburn and La Violette 1990; Perkins et al. 1990). Since horizontal temperature gradients of recent MAW in the gyres are significant in the horizontal density gradients, and these temperature gradients in the gyres result from the incoming temperature of AW at the Strait of Gibraltar, which is related with the upwelled waters in the Atlantic Ocean (Gascard and Richez 1985), it may be reasonable to infer that modifications in the surface temperature field incoming from the Strait of Gibraltar should influence the geostrophic balance of the flow in the western Alboran. We formulate the gyre maintenance problem as follows: the geostrophic circulation is closed in both gyres; this closed circulation is produced by the presence of light water in the core of both gyres; this light water is *geostrophically isolated* and, due to turbulent mixing, the density gradients in the gyres will decrease until they disappear. In other words, geostrophy alone cannot be responsible for the gyres maintenance for a long period of time. On the other hand, we have found, from salinity conservation, that surface water interchange between the cores of the gyres and the outside must occur, such circulation (if steady) being ageostrophic (as has been also shown by the preliminary ADCP data). Therefore the gyres, which are mainly in geostrophic balance, require that ageostrophic circulation or temporal variability take place for their maintenance. While this ageostrophic motion would be present at the western part of the WAG, vertical shear (on which baroclinic instability primarily depends) is relatively large at the north of the WAG. Here the strong zonal eastward flow (vertically oriented frontal surface with a large northward component of relative vorticity, U_z) evolves eastward to a more stable configuration, sloping the frontal zone and decreasing the geostrophic speed and horizontal geostrophic shear velocity. The role that the temporal variability caused by other observed phenomena plays in the above-described vorticity and shear configurations is, to a large extent, unknown. Some of these features are the short-term jet displacements (La Violette 1986), tide-induced fluctuations in the Strait of Gibraltar, transverse waves or oscillations of 9-day periods observed in the eastern flow, and splitting of the jet into several cores (Perkins et al. 1990).

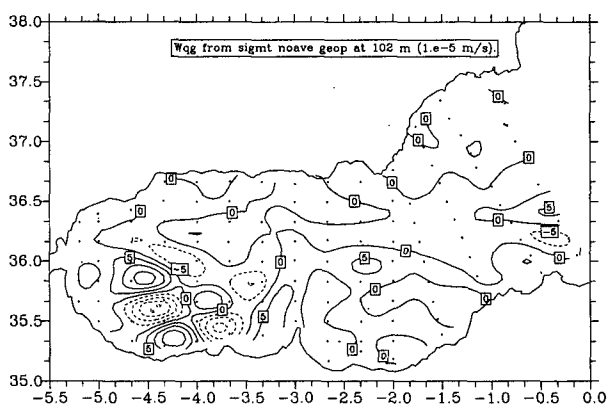

FIG. 25. Vertical velocity distribution at 100 m ($\Delta = 5 \times 10^{-5}$ m s^{-1}).

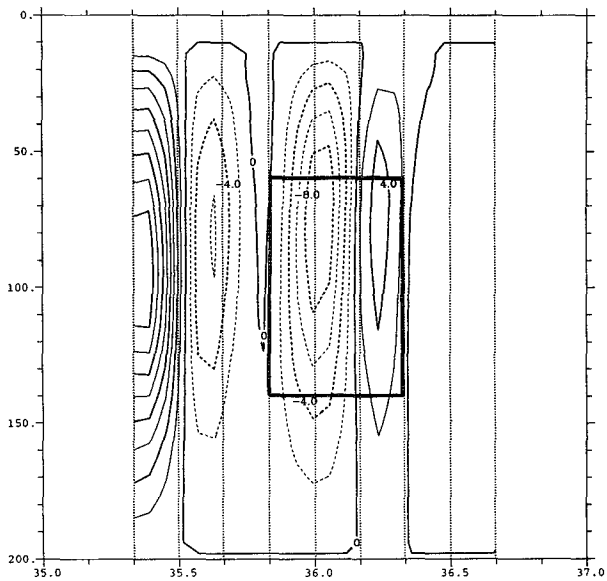

FIG. 26. Vertical velocity distribution between vertical sections D and E ($\Delta = 2 \times 10^{-5}$ m s^{-1}).

The above comments seem to indicate that the dynamics of the western Alboran is mainly frontal dynamics (more than in the eastern Alboran) where ageostrophic terms must be significant [the importance of the nonlinear terms in the western Alboran has been also the conclusion of several recent works (Perkins et al. 1990; Speich 1992)]. In the eastern Alboran new features also emerge from the data. The wavelike front does not acquire the large differences in salinity and temperature that characterize the Almería–Oran density front. This means that such a front is not the eastern boundary of the EAG; that is, the two phenomena are not necessarily related. Another interesting point concerns the two mesoscale cyclonic eddies. The existence of these two eddies in a similar position relative to the anticyclonic gyres seems to indicate that they are part of the same stable structure.

Acknowledgments. This work would not have been possible without the expertise of all the people inboard the R/V *García del Cid,* especially J. Font, J. Salat, M. Manríquez, E. G. Górriz, J. Sánchez, M. Lloret (ICM),

J.-M. Pinot, and A. Álvarez (UIB). J. L. López-Jurado (IEO) shared generously the CTD profiler. We thank also the courtesy of Moroccan and Algerian authorities and the Service Hydrographique of Algier. We thank J. Casanovas (UV) for processing the satellite images. D. Gomis (UIB) clarified aspects related to OI. We are also grateful for the comments of two anonymous reviewers. Partial support for this study was obtained through CICYT, AMB93-1046-CE, E.C. program MAST (MAS2-CT93-0066), and from the Office of Naval Research (RLH). One of the authors (AV) acknowledges a PFPI grant from the CICYT.

APPENDIX

Derivation of the Omega Equation for $N^2(x, y, z)$

The thermodynamic, hydrostatic, and vorticity equations are combined to cancel the height tendency terms in such a way that a generalized omega equation on an f plane, without friction and heating, is written as

$$\underbrace{\nabla^2(N^2w)}_{L_1} + f(\zeta_T + f)w_{zz} + \underbrace{f[\nabla w\cdot(-V_T, U_T)_z]_z}_{L_2}$$

$$\underbrace{-fw(\zeta_T)_{zz}}_{L_3} = \underbrace{f\nabla^2[\mathbf{V}_T\cdot(-V, U)_z]}_{R_1}$$

$$+ \underbrace{f(\mathbf{V}_T\cdot\nabla\zeta_T)_z}_{R_2} + f(\zeta_{ag})_{zt} \quad \text{(A1)}$$

(e.g., Pauley and Nieman 1992). Our objective is to express (A1) in such a way that analytical cancellation of terms does not occur. The horizontal velocity field $\mathbf{V}_T = \mathbf{V} + \mathbf{v}$ and the relative vorticity $\zeta_T = \zeta + \zeta_{ag}$ are decomposed into geostrophic plus ageostrophic components, the geostrophic velocity satisfying the "thermal wind" relation

$$(-V, U)_z = \nabla b, \quad \text{(A2)}$$

where $b \equiv g(f\rho_0)^{-1}\rho$, g is the acceleration of gravity, ρ is density, and ρ_0 is a mean constant density value. The ageostrophic velocity satisfies the continuity equation $u_x + v_y + w_z = 0$ since the geostrophic velocity is nondivergent ($U_x + V_y = 0$). The term by term decomposition is as follows:

$$L_1 = N^2\nabla^2 w + w\nabla^2N^2 + 2\nabla w\cdot\nabla N^2$$

$$L_2 = \underbrace{f\nabla w_z\cdot(-V, U)_z}_{L_{21}} + \underbrace{f\nabla w\cdot(-V, U)_{zz}}_{L_{22}}$$

$$+ f[\nabla w\cdot(-v, u)_z]_z$$

$$L_{22} = g\rho_0^{-1}\nabla w\cdot\nabla\rho_z = -\nabla w\cdot\nabla N^2$$

$$L_3 = \underbrace{-fw(\zeta_g)_{zz}}_{L_{31}} - fw(\zeta_{ag})_{zz}$$

$$L_{31} = g\rho_0^{-1}w(\rho_{xx} + \rho_{yy})_z = -w\nabla^2N^2$$

$$R_1 = \underbrace{f\nabla^2[\mathbf{V}\cdot(-V, U)_z]}_{R_{11}} + \underbrace{f\nabla^2[\mathbf{v}\cdot(-V, U)_z]}_{R_{12}+R_{13}}$$

$$R_{13} = -\mathbf{v}\cdot(\nabla\zeta_g)_z$$

$$R_2 = \underbrace{f(\mathbf{V}\cdot\nabla\zeta_g)_z}_{R_{21}} + \underbrace{f(\mathbf{V}\cdot\nabla\zeta_{ag})_z}_{R_{22}}$$

$$+ \underbrace{f(\mathbf{v}\cdot\nabla\zeta_g)_z}_{R_{23}} + \underbrace{f(\mathbf{v}\cdot\nabla\zeta_{ag})_z}_{R_{24}}$$

$$R_{22} = \mathbf{V}\cdot(\nabla\zeta_{ag})_z + U_zv_{xx} - U_zu_{yx} + V_zv_{xy} - V_zu_{yy}$$

$$R_{23} = \mathbf{v}\cdot(\nabla\zeta_g)_z + \mathbf{v}_z\cdot\nabla\zeta_g$$

$$R_{24} = \mathbf{v}\cdot(\nabla\zeta_{ag})_z + \mathbf{v}_z\cdot\nabla\zeta_{ag}.$$

Terms R_{11} and R_{21} can be written in a more simplificated way as two times the divergence of $\mathbf{Q}$ (Hoskins et al. 1978):

$$\mathbf{Q} \equiv (\mathbf{V}_x\cdot\nabla b, \mathbf{V}_y\cdot\nabla b).$$

After simplification the lhs and rhs of the generalized omega equation are written as

$$\text{LHS} = \nabla\cdot(N^2\nabla w) + f(\zeta_T + f)w_{zz}$$

$$+ \underbrace{f(u_{xx}V_z - v_{yy}U_z)}_{D_1} + \underbrace{f[\nabla w\cdot(-v, u)_z]_z}_{T_1} - fw(\zeta_{ag})_{zz},$$

$$\text{RHS} = 2f\nabla\cdot\mathbf{Q} + f\mathbf{V}_T\cdot(\nabla\zeta_{ag})_z + \underbrace{f(U_zv_{xx} - V_zu_{yy})}_{D_2}$$

$$+ f\mathbf{v}_z\cdot\nabla\zeta_g + \underbrace{f\mathbf{v}_z\cdot\nabla\zeta_{ag}}_{T_2} + f(\zeta_{ag})_{zt} + fR_{12}.$$

Terms D_1, D_2, and R_{13} can be written as two times the divergence of a vector $\mathbf{Q}_{ag}$:

$$\mathbf{Q}_{ag} \equiv (\mathbf{v}_x\cdot\nabla b, \mathbf{v}_y\cdot\nabla b),$$

and $\mathbf{Q}_T \equiv \mathbf{Q} + \mathbf{Q}_{ag} = [(\mathbf{V}_T)_x\cdot\nabla b, (\mathbf{V}_T)_y\cdot\nabla b]$. There is still some cancellation between terms T_1 and T_2 that can be avoided if $T_1 - T_2$ is expressed as

$$T_1 - T_2 = \nabla w\cdot(-v, u)_{zz} - (\nabla^2u, \nabla^2v)\cdot(-v, u)_z$$

to obtain

$$\nabla\cdot(N^2\nabla w) + f(\zeta_T + f)w_{zz} + f\nabla w\cdot(-v, u)_{zz} = 2f\nabla\cdot\mathbf{Q}_T + f(\nabla^2 U_T, \nabla^2 V_T)\cdot(-v, u)_z + f\,d(\zeta_{ag})_z/dt. \quad \text{(A3)}$$

At first order of approximation but keeping the N^2 terms [e.g., see Pauley and Nieman (1992) for a scaling discussion] the ageostrophic forcing is neglected in the rhs of (A3), the relative vorticity ζ_T is considered small in relation to planetary vorticity f, and terms including products of two ageostrophic factors are also neglected in the lhs of (A3) to obtain

$$\nabla\cdot(N^2\nabla w) + f^2 w_{zz} = 2f\nabla\cdot\mathbf{Q}. \quad \text{(A4)}$$

This equation can be derived in a more direct way from a generalized omega equation [in terms of the horizontal divergence of the ageostrophic horizontal pseudovorticity (Hoskins 1975)] by the substitution of geostrophic for total velocity gradients (Davies-Jones 1991), or from the generalized omega equation in terms of the ageostrophic relative vertical vorticity (Viúdez et al. 1996b). It should be noted that (A4) reduces to the usual quasigeostrophic omega equation if $N^2(x, y, z)$ is replaced by a mean profile $\bar{N}^2(z)$:

$$\bar{N}^2\nabla^2 w + f^2 w_{zz} = 2f\nabla\cdot\mathbf{Q}. \quad \text{(A5)}$$

REFERENCES

Akima, H., 1978: A method of bivariate interpolation and smooth surface fitting for values given at irregularly distributed points. *ACM-TOMS,* **4**(2), 148–159.

——, 1984: On estimating partial derivatives for bivariate interpolation of scattered data. *Rocky M. J. Math.,* **14,** 41–52.

Arnone, R. A., D. A. Wiesenburg, and K. D. Saunders, 1990: The origin and characteristics of the Algerian Current. *J. Geophys. Res.,* **95,** 1587–1598.

Atkinson, K. E., 1988: *An Introduction to Numerical Analysis.* 2d ed. Wiley and Sons, 693 pp.

Bower, A. S., 1989: Potential vorticity balances and horizontal divergence along particle trajectories in Gulf Stream meanders east of Cape Hatteras. *J. Phys. Oceanogr.,* **19,** 1669–1681.

Brathset, A. M., 1986: Statistical interpolation by means of successive correction. *Tellus,* **38A,** 439–447.

Bray, N. A., and N. P. Fofonoff, 1981: Available potential energy for MODE eddies. *J. Phys. Oceanogr.,* **11,** 30–47.

Cano, N., and F. F. de Castillejo, 1972: Contribución al conocimiento del Mar de Alborán III. Variaciones del remolino anticiclónico. *Bol. Inst. Esp. Oceanogr.,* **157,** 3–7.

Cheney, R. E., 1978: Recent observations of the Alboran Sea frontal system. *J. Geophys. Res.,* **83,** 4593–4597.

——, and R. A. Doblar, 1982: Structure and variability of the Alboran Sea frontal system. *J. Geophys. Res.,* **87,** 585–594.

Chew, F., J. M. Bane, and D. A. Brooks, 1985: On vertical motion, divergence, and the thermal wind balance in cold-dome meanders: A diagnostic study. *J. Geophys. Res.,* **90,** 3173–3183.

Davies-Jones, R., 1991: The frontogenetical forcing of secondary circulations. Part I: The duality and generalization of the Q-vector. *J. Atmos. Sci.,* **48,** 497–509.

Donde Va? Group, 1984: Donde Va? An oceanographic experiment in the Alboran Sea. The oceanographic report. *Eos, Trans. Amer. Geophys. Union,* **65,** 682–683.

Donguy, J. R., 1962: Hydrologie en mar d'Alboran. *Cah. Oceanogr.,* **14,** 573–578.

Franke, R., 1988: Statistical interpolation by iteration. *Mon. Wea. Rev.,* **116,** 961–963.

Gascard, J. C., and C. Richez, 1985: Water masses and circulation in the western Alboran Sea and in the Straits of Gibraltar. *Progress in Oceanography,* Vol. 15, Pergamon, 157–216.

Heburn, G. W., and P. E. La Violette, 1990: Variations in the structure of the anticyclonic gyres found in the Alboran Sea. *J. Geophys. Res.,* **95,** 1599–1613.

Holton, J. R., 1979: *An Introduction to Dynamic Meteorology.* 2d ed. Academic Press, 391 pp.

Hoskins, B. J., 1975: The geostrophic momentum approximation and the semigeostrophic equations. *J. Atmos. Sci.,* **32,** 233–242.

——, I. Draghici, and H. C. Davies, 1978: A new look at the ω-equation. *Quart. J. Roy. Meteor. Soc.,* **104,** 31–38.

Lanoix, F., 1974: Projet Alboran, Etude hydrologique et dynamique de la Mer d'Alboran. Tech. Rep. 66, NATO, Brussels, 39 pp. plus 32 figs.

La Violette, P. E., 1986: Short-term measurements of surface currents associated with the Alboran Sea during Donde Va? *J. Phys. Oceanogr.,* **16,** 262–279.

——, 1990: The Western Mediterranean Circulation Experiment (WMCE): Introduction. *J. Geophys. Res.,* **95,** 1511–1514.

Millard, R. C., W. B. Owens, and N. P. Fofonoff, 1990: On the calculation of the Brunt–Väisäla frequency. *Deep-Sea Res.,* **37,** 167–181.

Paige, C. C., and M. A. Saunders, 1975: Solution of sparse indefinite systems of linear equations. *SIAM J. Num. Anal.,* **12,** 617–629.

Palmen, E., and C. W. Newton, 1969: *Atmospheric Circulation Systems.* Academic Press, 603 pp.

Parrilla, G., and T. H. Kinder, 1987: The physical oceanography of the Alboran Sea. NORDA Rep. 184, 26 pp.

Pauley, P. M., and S. J. Nieman, 1992: A comparison of quasigeostrophic and nonquasigeostrophic vertical motions for a model-simulated rapidly intensifying marine extratropical cyclone. *Mon. Wea. Rev.,* **120,** 1108–1134.

Perkins, H., T. Kinder, and P. E. La Violette, 1990: The Atlantic inflow in the western Alboran Sea. *J. Phys. Oceanogr.,* **20,** 242–263.

Pollard, R. T., and L. Regier, 1992: Vorticity and vertical circulation at an ocean front. *J. Phys. Oceanogr.,* **22,** 609–625.

Seco, E., 1959: La capa de velocidad cero en el mar de Alborán. *Rev. CENIC Ceinc. Biol.,* **25,** 765–779.

Speich, S., 1992: Étude du forçage de la circulation océanique par les détroits: cas de la mer d'Alboran. Doctoral dissertation, Université Paris VI, 245 pp.

Tintoré, J., P. E. La Violette, I. Blade, and A. Cruzado, 1988: A study of an intense density front in the eastern Alboran Sea: The Almería–Oran Front. *J. Phys. Oceanogr.,* **18,** 1384–1397.

——, D. Gomis, S. Alonso, and G. Parrilla, 1991: Mesoscale dynamics and vertical motion in the Alboran Sea. *J. Phys. Oceanogr.,* **21,** 811–823.

Viúdez, A., and J. Tintoré, 1995: Time and space variability in the eastern Alboran Sea from March to May 1990. *J. Geophys. Res.,* **100,** 8571–8586.

——, R. L. Haney, and J. Tintoré, 1996a: Circulation in the Alboran Sea as determined by quasi-synoptic hydrographic observations. Part II: Mesoscale ageostrophic motion diagnosed through density dynamical assimilation. *J. Phys. Oceanogr.,* **26,** 706–724.

——, J. Tintoré, and R. L. Haney, 1996b: About the nature of the generalized omega equation. *J. Atmos. Sci.,* **53,** 787–795.

Werner, F. E., A. Cantos-Figuerola, and G. Parrilla, 1988: A sensitivity study of reduced-gravity channel flows with application to the Alboran Sea. *J. Phys. Oceanogr.,* **18,** 373–383.